2014

# Measurement Of Optical Properties Of Soot Using Cavity Ring-Down Spectroscopy And Integrating Nephelometry

Damon M. Smith
*North Carolina Agricultural and Technical State University*

# Measurement of Optical Properties of Soot Using Cavity Ring-Down Spectroscopy and Integrating Nephelometry

Damon M. Smith

North Carolina A&T State University

A thesis submitted to the graduate faculty

in partial fulfillment of the requirements for the degree of

MASTER OF SCIENCE

Department: Physics

Major: Physics

Major Professor: Dr. Solomon Bililign

Greensboro, North Carolina

2014

The Graduate School
North Carolina Agricultural and Technical State University

This is to certify that the Master's Thesis of

Damon M. Smith

has met the thesis requirements of
North Carolina Agricultural and Technical State University

Greensboro, North Carolina
2014

Approved by:

| | |
|---|---|
| Dr. Solomon Bililign<br>Major Professor | Dr. Yuh-Lang Lin<br>Committee Member |
| Dr. Abdellah Ahmidouch<br>Department Chair | Dr. Liam Duffy<br>Committee Member |

Dr. Sanjiv Sarin
Dean, The Graduate School

## Biographical Sketch

Damon M. Smith is a research assistant at North Carolina Agricultural and Technical University working on his Master of Science in Physics. He also has a Bachelor of Science in Computer Science and Mathematics from High Point University, where he currently works as an adjunct professor in their physics department. Damon has a wife, Tonya, a son, Zechariah, and another baby due in March. He enjoys helping others through teaching and serves regularly at his church in Kernersville.

# Dedication

This work is dedicated to my wife, Tonya, for her constant encouragement and support, and to my kids, both present and future, to encourage them to pursue their goals.

# Acknowledgments

I would like to thank Dr. Solomon Bililign for his guidance, support, and encouragement throughout this process. He has been an excellent teacher and always believed in my success. Dr. Marc Fiddler, Sujeeta Singh, and Getachew Tedla also contributed to this work and taught me how to use everything in the lab. There were many other contributions made by our numerous REU students, specifically Isabel D. Colón-Bernal, who helped greatly with field work.

This work is supported by the Department of Defense under grant #W911NF-11-0188.

Table of Contents

List of Figures

# List of Tables

## Abstract

Since black carbon and brown carbon are among the greatest contributors to radiative forcing (black carbon being second only to carbon dioxide), this work focuses on the laboratory measurement of their optical properties using cavity ring-down spectroscopy (CRDS) and integrating nephelometry. Water soluble soot is collected using an impinger and cascade impactor by burning different fuel types to mimic ambient aerosols dominant in regions where biomass burning is the main source of aerosols. Using an optical parametric oscillator (OPO) as a light source, we are able to measure extinction and scattering over a wide range of wavelengths. A correction factor is calculated using a method by Anderson and Ogren to reconcile scattering from the nephelometer to extinction from the CRDS. The extinction-minus-scattering method is then used to determine absorption. Purely scattering polystyrene latex (PSL) spheres of known sizes (100 – 700 nm) are used in the lab to calibrate the system for this study. Measurements of optical properties of soot collected from different fuel sources at different stages of burning are reported.

# CHAPTER 1

## Introduction and Background

Solar radiation is the primary source of energy for life on our planet. The amount of radiation that reaches the earth's surface is called the radiation budget, measured in watts per meter squared ($W/m^2$). Too much fluctuation one way or the other may lead to global warming or cooling. Radiation may be scattered or absorbed by anything in its path, either particles in the air, or the earth's surface itself. Scattered radiation is generally reflected back into space, leading to a cooling effect. Absorbed radiation is generally reemitted as infrared radiation, or heat, leading to a warming effect. This study is primarily concerned with the contribution of soot aerosols, created by biomass burning, to the scattering or absorbing of radiation in the atmosphere. This is accomplished by measuring the optical properties of the soot (its ability to scatter or absorb radiation) in a laboratory setting. This information can then be used in climate models and for accurate interpretation of remote sensing measurements.

### 1.1 Description of Aerosols

An aerosol can be any particulate matter suspended in a gas. Aerosols have many different physical and chemical properties, such as size, shape, and index of refraction, which affect their ability to scatter or absorb light. The size of an aerosol can vary greatly, anywhere from a few nanometers to over fifteen micrometers in diameter. Aerosols with sizes smaller than 50 nanometers either spread out too quickly to make much of an impact or form into larger aerosols through agglomeration. Aerosols much bigger than 2 μm have short lifetimes in the atmosphere due to gravitational settling. However, aerosols between these ranges can stay in the atmosphere for up to a few weeks.

This extended lifetime gives aerosols the opportunity to have far-reaching effects as they stay airborne longer; they even have the potential to travel across continents. Sometimes, the hazy conditions experienced in North America are actually the result of sand, sea salt, or soot aerosols from another continent. This longer lifetime also means that the contributions of aerosols can have a long-term effect on the climate of a region. They affect the climate directly by scattering or absorbing light and indirectly through the formation of clouds, which in turn scatter or absorb light. As shown in Figure (1), the uncertainty of these effects is one of the biggest unknowns for modeling radiative forcing (IPCC 2013). This study focuses on aerosols in the range of 100 to 700 nm. Aerosols near 100 nm or below begin to experience scattering differently as will be explained below.

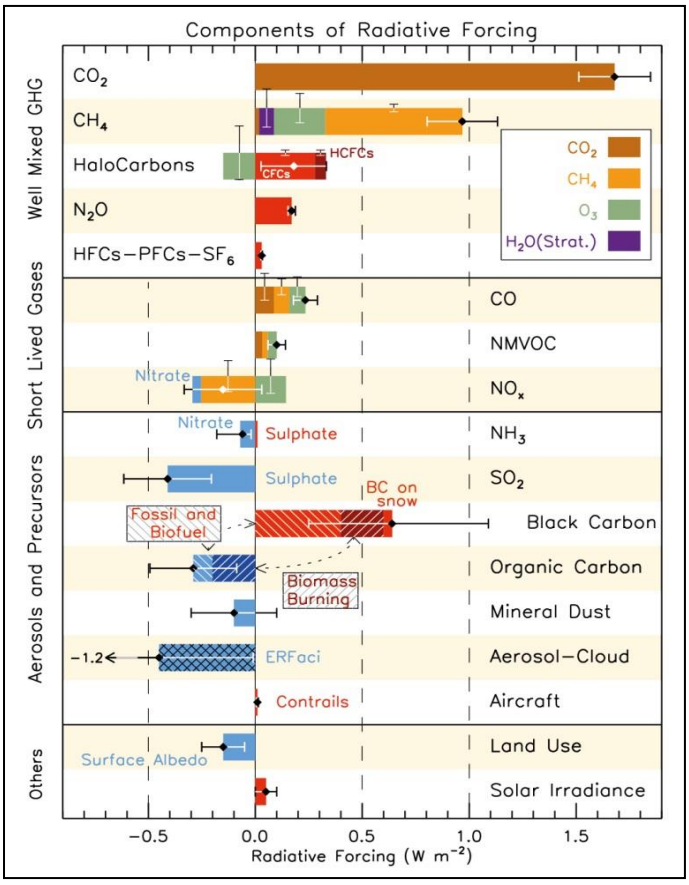


*Figure 1*. Contribution to radiative forcing of greenhouse gasses and aerosols (IPCC 2013).

The shape of aerosols can vary greatly, making it difficult to determine the dependence of optical properties on their shape. As light strikes different sides of the aerosol, it is presented with different geometrical cross sectional areas depending on the orientation of the aerosol. Our current equipment is only able to determine the maximum diameter of the given orientation for the aerosol, giving an upper limit to the cross sectional areas measured, which will be discussed in a later chapter.

### 1.2 Sources of Aerosols

Aerosols can come from natural sources, such as wild fires, or anthropogenic sources, such as cooking, manufacturing, or agricultural burning. Although aerosols can be produced in many ways, this study focuses on aerosols produced through biomass burning, using wood as a primary source of soot aerosol. In recent controlled emission studies of biomass burning, Yokelson et al. (2013) discovered several hundred chemicals and particulates. Many of these particulates are poorly understood. As we better understand these particulates, we can better estimate their contribution to the cooling or warming of the atmosphere.

### 1.3 Importance of Aerosols in the Atmosphere

Although aerosol particles can have adverse effects on the health of living organisms, of particular interest in this study are the optical properties of aerosols, as this describes their effects on the earth's radiation budget. This effect has the potential to disrupt the natural climate. Aerosols interact with this radiation by either scattering (reflecting) or absorbing the incoming light. Soot aerosol is primarily absorbing in nature and reemits radiation in the infrared as heat, causing a warming effect on the earth. Other aerosols may be more reflective and scatter light instead, leading to a cooling effect on the earth. Although it is known that aerosols behave in this

way and contribute to global warming and cooling, the uncertainty of these contributions is still fairly large (IPCC 2013).

A highly absorbing aerosol, such as black carbon, would increase the temperature of the atmosphere as it absorbs radiation. With less radiation available to reach the earth's surface, the temperature of the ground decreases. This difference in temperature prevents evaporation, causing a decline in cloud formation, which in turn leads to less rainfall (Bond et al. 2013). Another detrimental effect happens when a highly absorbing aerosol mixes with snow. The snow then absorbs more radiation than it would have normally and melts faster, leading to increased flooding in some regions (Hansen et al. 2004). More recent studies (Wang et al 2013; Saide et al. 2014; Yuan 2014) have also linked aerosols with severe weather.

Aerosols can influence climate indirectly as they serve as cloud condensation nuclei but they can also change climate by absorbing or scattering radiation. Among the aerosols black carbon is recognized as one of the greatest contributors to global warming (Bond et al. 2013). It is important to take accurate measurements of aerosol optical properties over the entire solar (Ramanathan et al. 2007) spectrum in order to quantify the impact of aerosols on climate and severe weather. It is for these reasons that we are attempting to increase the body of knowledge concerning aerosols and their optical properties.

**1.4 Optical Properties of Aerosols**

The extinction coefficient, $\alpha_{ext}$, of an aerosol measures the attenuation or gradual loss in the intensity of light. It has units of $m^{-1}$ and is given by equation (1), where $\sigma_{ext}$ is the cross section and $N$ is the number density ($N = n/V$) of the aerosol. Similar equations can be used in determining the scattering and absorption coefficients.

$$\alpha_{ext} = \sigma_{ext} N_{ext} \quad (1)$$

These coefficients may also be determined from Beer-Lambert's law, given in equation (2), where $I$ is the intensity, $I_0$ is the initial intensity, and $r$ is the distance traveled through the medium. This gives us the loss in intensity of light. As the distance traveled, $r$, increases, the intensity is lost exponentially. The extinction coefficient is the value that we will measure experimentally in our cavity ring-down system, which will be further explained in the second chapter.

$$I = I_0 e^{-\alpha_{ext} r} \tag{2}$$

The single scattering albedo (ω) of an aerosol measures its ability to scatter light versus absorb light. The value of ω is always between 0 and 1. If ω = 1, the particle is purely scattering, but if ω = 0, the particle is purely absorbing. This value can be determined by dividing the scattering cross section of the aerosol by its extinction cross section as in equation (3).

$$\omega = \frac{\sigma_{scat}}{\sigma_{ext}} = \frac{\sigma_{scat}}{\sigma_{scat}+\sigma_{abs}} = \frac{\alpha_{scat} N_{ext}}{\alpha_{ext} N_{scat}} \tag{3}$$

Here it can be noted that extinction is equal to scattering plus absorption, which is a useful relationship. It should also be noted that while the number densities should be the same in the above equation and cancel out, these are usually measured separately in the lab and will give different results depending on particle loss throughout the system.

It is also interesting to know whether these properties are wavelength dependent on the incoming radiation. This dependency is called the Ångstrom coefficient and is given in equation (4). The Ångstrom coefficient may also be used to extrapolate the scattering coefficients to wavelengths beyond the range of our equipment. Specifically, the nephelometer used in this study only took measurements at three specific wavelengths (450, 550, and 700 nm), so extrapolating the data was necessary to compare results with data gathered from the cavity ring-down system.

$$å = -\frac{\log\frac{\alpha(\lambda_1)}{\alpha(\lambda_2)}}{\log\frac{\lambda_1}{\lambda_2}} \quad (4)$$

Another important quantity relates the cross section of extinction, scattering, or absorbing to the actual geometric cross sectional area. This is called the efficiency of scattering, and is given by equation (5), where $A = \pi r^2$ for a spherical particle. The geometric cross sectional area can be thought of as the shadow cast by the particle if a beam of light is shining on it; it is only a two-dimensional shape.

$$Q = \frac{\sigma}{A} \quad (5)$$

**1.5 Definition of Black Carbon**

Black carbon (BC) is one of the primary contributors to absorption in the atmosphere and the effects of global warming, due to its mostly absorbing qualities. The terms "soot", "black carbon" and "elemental carbon", among others, are often confused and used interchangeably, even though they have distinctly different meanings. In general, black carbon refers to primarily light-absorbing carbonaceous material (Moosmüller 2009). More recently, black carbon has been given a very stringent list of properties that it must possess in order to be called "black carbon". The following quote from Petzold et al. (2013) gives these properties as summarized from Bond et al. (2013):

> "…BC is characterized by the following distinct properties: (1) it strongly absorbs visible light, with a MAC [mass absorption cross section] value above 5 $\mathrm{m^2 g^{-1}}$ at a wavelength $\lambda = 550$ nm for freshly produced particles; (2) it is refractory, with a volatilization temperature near 4000 K; (3) it is insoluble in water, in organic solvents including methanol and acetone, and (4) it

> consists of aggregates of small carbon spherules of <10 nm to approximately 50 nm in diameter. In order to include a distinct microstructural feature, we add a fifth property saying that (5) it contains a high fraction of graphite-like $sp^2$-bonded carbon atoms…"

By this definition, the soot samples collected in this phase of our work would not be considered black carbon, in violation of the third property. As will be described in more detail in the third chapter, our current solution consists of distilled water.

Other important synonyms of "black carbon" include "elemental carbon", "ns-soot" (a relatively new term coined by Buseck et al. (2012)), and "soot" or "soot carbon" (Petzold et al. 2013). Elemental carbon simply refers to any particulate matter that is mostly carbonaceous, with little to no bonding with other elements. Ns-soot particles, short for nanosphere-soot, exist between 10 and 100 nm, and are the building blocks of soot aggregates. When viewed under a microscope, it can be seen that the fractal patterns of these aggregates can be subdivided into smaller spherical structures. This can be seen in Figure (2), where we were able to view our samples using a scanning electron microscope. However, as these ns-soot particles form into bigger and bigger aggregates, they exceed the size range of our equipment. Instead, we are primarily looking at the last category mentioned above, soot, which contains carbon produced from the combustion of fossil fuels, with small contributions by hydrogen and oxygen. Although this definition excludes any organic species present during combustion, we currently have no way to separate these in the laboratory, so it is possible that they may be included in our findings.

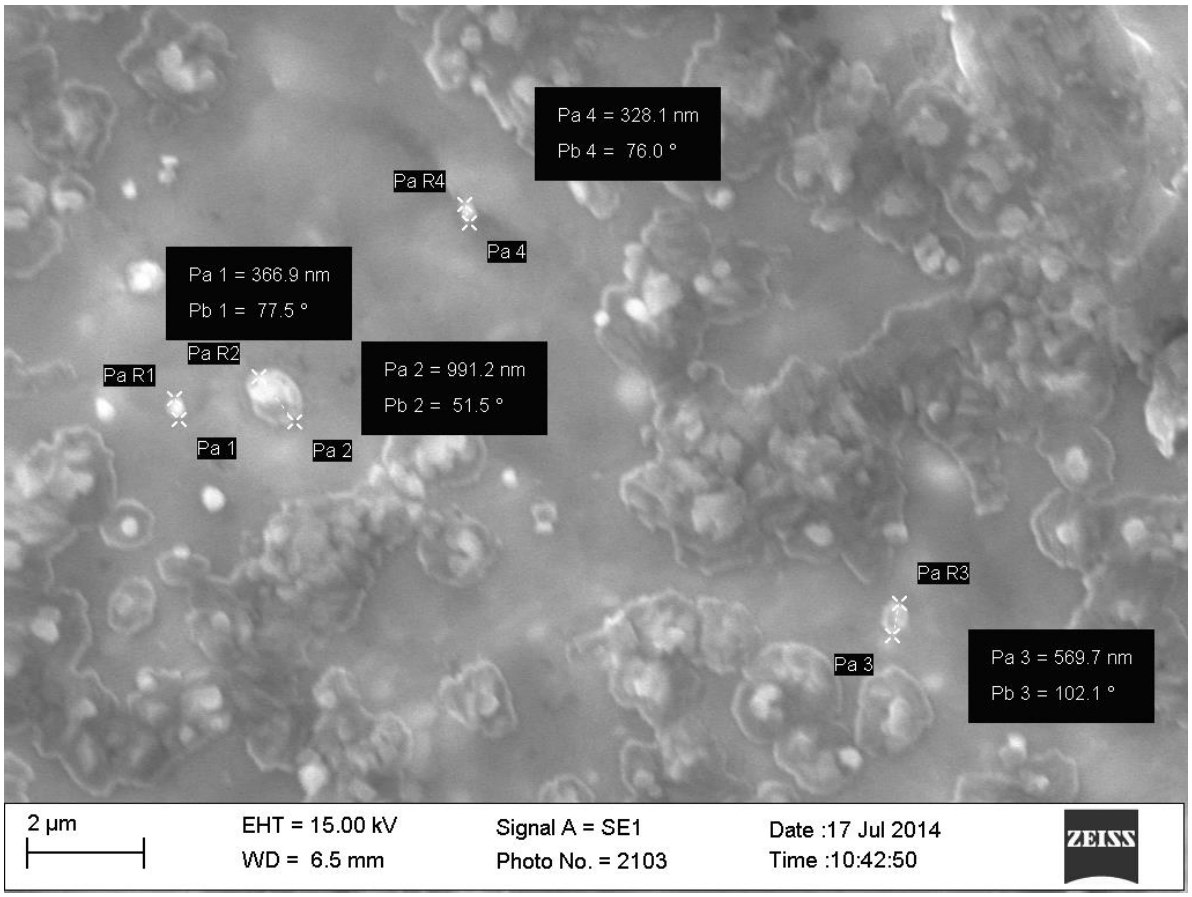


*Figure 2.* Scanning electron microscope image of soot aerosol during the smoldering stage.

No matter which definition is used, it is strongly recommended that any references to "black carbon", "soot", etc., be further clarified based on the experimental methods used and the application. For the remainder of this paper, we will use the words "soot", "soot particle(s)", or "soot aerosol(s)" interchangeably to define the particulate matter being studied. These particles were produced from the combustion of various types of wood. It is assumed that the majority of these particles are absorbing; however, other organic compounds may be present, which would affect the absorption of the sample as a whole. The words "aerosol(s)" and "aerosol particle(s)" will continue to describe any aerosol in general. Although this work focuses on soot aerosol, any aerosol between 100 and 700 nm may be measured using our system.

### 1.6 Biomass Burning as a Source of Soot Aerosols

Biomass burning is the combustion of living and/or dead vegetation that is initiated by humans or lightning. The most significant form of biomass burning in the USA is wood burning. The Environmental Protection Agency (EPA) (EPA 1986) in 1984 estimated that there were 11 million U.S. wood burning stoves, that they burned 43 million tons for woodstoves annually, that fireplaces burned an additional 11 million tons, and industry another 2 million tons of wood. Many third-world nations use wood, straw, dung, leaves, or other materials for heating and cooking food. Worldwide, huge amounts of biomass are burned in tropical rain forests in South America, Africa, and Malaysia/Indonesia to make room for agricultural crops (Curtis 2002).

Most recent studies point to the potent source of human-induced climate warming: aerosol particles emitted by biomass burning (Bond et al. 2013. IPCC 2013, Wang et al. 2013). The recent estimate (IPCC 2013) of biomass aerosol radiative forcing is 50% larger than earlier estimates.

The combustion of wood is a complex process. Wood is generally considered to burn in three distinct, but overlapping stages (Tillman 1981). The first stage, ignition, involves use of heat to drive off moisture and bring the wood to the pyrolysis temperature. In the second stage, flaming, the wood undergoes pyrolysis (thermal decomposition under oxygen-poor conditions) when it reaches around 500-600°F. This process leads to production of organic gases with increasing high molecular weight as combustion progresses. The remaining portion is charcoal, which burns at about 1100°F. Once volatiles are driven off, direct combustion of black carbon occurs in the third stage, smoldering. Any unburned gas-phase residue will be in the form of smoke or condensed pyrolysis gases. Complete combustion requires plenty of oxygen and the three elements of temperature, turbulence, and time.

The combustion technique as well as operational parameters such as fuel load, airflow setting, and the fuel itself has an important influence on the amount and the composition of particle emissions (Schmidl 2011; Fine et al. 2001; 2002; 2004 a, b). Soot is formed from organic precursors in zones of high temperatures and lack of oxygen, where volatiles and primary tars react to form secondary tars and polyaromatic hydrocarbons, which can subsequently form soot particles by further agglomeration and release of hydrogen (Schwartz and Lewis 2012).

**1.7 Purpose of Thesis**

The focus of this study was to continue the efforts of previous work in the calibration of a cavity ring-down and nephelometry system to make it usable for measuring the optical properties of soot aerosols that mimic ambient aerosols where biomass burning is a major source of soot (Singh et al. 2014). Earlier measurements of aerosol optical properties (Radney et al. 2009, Moosmuller et al. 2005, Pettersson et al. 2004) have been confined to a specific range of light wavelength, usually around 532 nm. Our setup allows us to scan over a wide range of wavelengths to mimic the solar spectrum in order to better understand the optical properties of aerosols. The work presented here used the extinction minus scattering technique where extinction is measured using a cavity ring down system and scattering is measured using an integrating nephelometer. This will be further explained in the second and third chapters.

Currently, most remote sensing applications do not measure the optical properties of individual species within an aerosol volume, but only of the aerosol as a whole. That is why it is important to study aerosols in a laboratory setting where the components can be separated and analyzed individually. This would allow us to accurately interpret remote sensing data. Our laboratory setup is very flexible and gives us the ability to quickly measure the optical properties

of several samples over a given wavelength range. This range can also be adjusted without too much difficulty by replacing several mirrors in the optical setup and their corresponding dye in the dye laser (if used instead of the optical parametric oscillator).

In chapter two, the different types of scattering are discussed, specifically Rayleigh and Mie scattering, including several methods to measure the cross sections. In chapter three, the experimental setup is described in detail, and includes: soot aerosol collection, laboratory setup, and data collection. Results comparing scattering spheres, absorbing spheres, and soot particles at a size of 400 nm are presented in chapter four, and conclusions are reported in chapter five.

# CHAPTER 2

## Measurement of Optical Properties

### 2.1 Reflection and Refraction

When a wave, such as electromagnetic radiation, is incident on a surface, part of the wave is reflected from the surface and part is transmitted through the surface of the second medium at a refracted angle. The reflected angle is equal to the incident angle and the refracted angle can be calculated from Snell's Law ($n_1 \sin\theta_1 = n_2 \sin\theta_2$) if the refractive index, *n*, of each of the media is known. This index is equal to the ratio of the speed of light in a vacuum to the speed of light in the medium ($n = c/v_{medium}$). If $n_2$ is bigger than $n_1$, the reflected wave is inverted at the boundary between the two media or shifted 180° out of phase; otherwise, it remains upright and in phase with the original wave.

For absorbing particles, the index of refraction becomes complex. It is expressed as $\tilde{n} = n + i\kappa$, where $\kappa$ is related to the permittivity of the medium. In this case the incoming wave is split into three parts: reflection (scattering), refraction (transmission), and absorption. If a wave is absorbed and immediately reemitted, this can also be considered as scattering. The absorption coefficient can now be given by equation (6).

$$\alpha_{abs} = \frac{4\pi\kappa}{\lambda_0} \tag{6}$$

The above theory holds as long as the wavelength of the radiation is small when compared to the size of the surface it is coming into contact with. When the wavelength is similar in size to the diameter of an aerosol particle (when considering spherical particles) or some other size parameter (when considering non-spherical particles), the method of reflection and refraction is not as straight-forward.

When electromagnetic radiation is reflected from many different surfaces, as it does when traveling through an aerosol, the result is called scattering. This scattering is generally divided into three categories based on an equal-volume-sphere size parameter, $X = \pi D_p/\lambda$, where $D_p$ is the diameter of a single particle and λ is the wavelength of the radiation. When $X \gg 1$, the particle is much bigger than the wavelength, normal geometry applies, and reflection and refraction happen as described above. When $X \ll 1$, the wavelength is much bigger than the particle, and Rayleigh theory applies, which will be described below. For all other values of $X$ in the middle range near 1, the particle and the wavelength are comparable to each other in size and Mie theory applies, which will also be described below. These theories are all based on the solutions of the spherical wave equation for the scattering of electromagnetic radiation by a sphere.

**2.2 Mie Theory**

Gustav Mie (1908) showed that the solutions of the wave equations with spherical boundary conditions could be found in terms of an infinite series of magnetic and electric poles. Equations (7) through (9) give these solutions for the extinction, scattering, and absorption cross sections. (Bohren, and Huffmann, 2010).

$$\sigma_{ext} = \frac{\pi {D_p}^2}{2X^2} \sum_{n=1}^{\infty} (2n+1)[-\mathrm{Re}(a_n + b_n)] \quad (7)$$

$$\sigma_{scat} = \frac{\pi {D_p}^2}{2X^2} \sum_{n=1}^{\infty} (2n+1)(|a_n|^2 + |b_n|^2) \quad (8)$$

$$\sigma_{abs} = \sigma_{ext} - \sigma_{scat} \quad (9)$$

The last equation describes the relationship between extinction, scattering and absorption. If both extinction and scattering are known, then absorption is easily found. The terms $a_n$ and $b_n$ are the magnetic and electric multipoles of order *n*, where $\psi$ and $\xi$ are the Riccati-Bessel

functions, *j* represents the Bessel functions, and *h* represents the Hankel functions. These are given in equations (10) through (13). These are actually quite complicated to calculate and were not easily attained when Mie first formulated the theory. It is now easy to perform these calculations using computer algorithms.

$$a_n = \frac{m\psi_n(mx)\psi_n'(x) - \psi_n(x)\psi_n'(mx)}{m\psi_n(mx)\xi_n'(x) - \xi_n(x)\psi_n'(mx)} \tag{10}$$

$$b_n = \frac{\psi_n(mx)\psi_n'(x) - m\psi_n(x)\psi_n'(mx)}{\psi_n(mx)\xi_n'(x) - m\xi_n(x)\psi_n'(mx)} \tag{11}$$

$$\psi_n(mx) = mxj_n(mx) \tag{12}$$

$$\xi_n(mx) = mxh_n^{(1)}(mx) \tag{13}$$

This theory is good only if the particles are pure spheres. For non-spherical particles, we can use the so called T-matrix method. This method, developed by Waterman (Mishchenko et al. 1996), is kept up to date by Mishchenko et al. (2013). We did not use the T-Matrix method in this work even though the soot aerosols are non-spherical. Approximate results can be obtained using Mie theory.

**2.3 Rayleigh Theory**

Rayleigh theory applies in the range where the diameter of the particle is about one tenth of the wavelength of the incoming radiation or smaller. For the visible spectrum (~400-700nm), this would happen for sizes less than or equal to 50 nm. Experimentally, it was found that even particles up to 100 nm can be approximated fairly accurately using this kind of scattering.

Rayleigh theory is only an approximation of the more general Mie theory. Only the lowest order terms of $a_n$ and $b_n$ are considered. Most of those become zero, leaving only the $b_1$ term. This term reduces to equation (14), which then gives the Rayleigh cross sections as equations (15) and (16), where $\tilde{n}$ is the complex index of refraction of the aerosol particles as

defined above. Rayleigh scattering is dominated by the $\lambda^{-4}$ term. Since this cross section depends on the wavelength of light, shorter wavelengths are scattered more than longer wavelengths. Since the wavelength of blue light is smaller than the wavelength of red light, blue light has a larger cross section, meaning it scatters more than red light, which is why the sky appears blue during the day.

$$b_1 = -\frac{2i}{3}\left(\frac{\tilde{n}-1}{\tilde{n}+2}\right)X^3 \tag{14}$$

$$\sigma_{ext} = \frac{\pi^2 {D_p}^3}{\lambda}\,\mathrm{Re}\left(\frac{\tilde{n}-1}{\tilde{n}+2}\right) \tag{15}$$

$$\sigma_{sca} = \frac{2\pi^5 {D_p}^6}{3\lambda^4}\left(\frac{\tilde{n}^2-1}{\tilde{n}^2+2}\right)^2 \tag{16}$$

**2.4 Comparison of Measurement Techniques**

Several methods are available for measuring the various coefficients (extinction, scattering, and absorption). The first general category is filter-based methods (Hansen et al., 1982). These involve collecting aerosol on a filter and determining the absorption coefficient by measuring the transmission of light through the filter. This method is very inexpensive, making it the most widely used method; however, this method suffers from artifacts and does not take scattering into account. This means that the resultant measurement is really extinction and the absorption is consistently high (Schmid et al., 2006; Müller et al., 2011; Collaud-Coen et al., 2010). Although corrections may be applied, accuracies of this method range between 20 and 30%, though some may be as low as 12%. These corrections are usually based on laboratory-generated particles, which could limit their usefulness (Bond et al. 2013).

Another popular method, which is very accurate for measuring absorption, is the photoacoustic spectrometer (PAS) (Arnott et al. 1999; Lack et al. 2006, Ajtai et al. 2010, Sharma et al. 2013). In this method, particles within a cavity absorb energy from a laser. When this

energy is absorbed, the temperature of the particles increases, causing increased vibrations of the aerosol particles. These vibrations create an increase in the pressure of the gas containing the aerosol, producing acoustic waves which can then be measured by a very sensitive microphone. The uncertainty of the absorption measured using this method is only 5% (Bond et al. 2013); however, the equipment involved can be very costly.

The method chosen for this work is the extinction-minus-scattering method, using cavity ring-down spectroscopy (CRDS) to measure extinction, combined with integrating nephelometry to measure scattering (Moosmüller et al. 2009; Bond, and Bergstrom 2006, Gerber, 2009). There are two main advantages to using this method. The first is that the equipment is less expensive than the PAS system. The second advantage comes from the fact that the effective path length of the cavity is much longer than the physical length of the cavity, due to a single laser pulse making multiple passes through the same sampling volume. CRDS is well-characterized and can be used for making absolute measurements. Further detail is given in the next section.

**2.5 Cavity Ring-Down Spectroscopy**

Cavity ring-down spectroscopy was first developed by Deacon and O'Keefe (O'Keefe et al. 1988, Zalicki and Zare 1995,), to measure the concentration of gases. It has since been used by other groups (Riziq et al. 2007, Radney et al. 2009, Pettersson et al. 2004, Moosmüller et al. 2005, Baynard et al. 2007 ) in the measurement of aerosol optical properties.

The laboratory setup includes a cavity having highly reflective mirrors at each end, coupled with a pulsed laser. 99.99% of the laser pulse is reflected before entering the cavity, but the part that does makes it inside is effectively trapped, with only a small portion escaping with each pass of the laser. With each pass, only a fraction of the original intensity escapes the cavity

to be measured by a photomultiplier tube. The intensity decreases exponentially, and the time that it takes to reach 1/e of the original amount, called the ring-down time ($\tau_0$), can be calculated. This is the effective photon lifetime in the cavity. When an aerosol is introduced into the cavity, the ring-down time ($\tau$) is shortened, due to the additional scattering and absorbing of light by the aerosol particles. This difference can be used to find the extinction coefficient of the aerosol and, subsequently, its extinction cross section, as given in equation (17), where $c_{air}$ is the speed of light in air and $R_L$ is the ratio of the mirror-to-mirror distance to the length of the cavity occupied by the sample. The sample is separated from the mirrors by a small purge flow of nitrogen, to keep the aerosol from building up on the mirrors. Here, the number density is the average number of particles in the cavity at any given time. As mentioned previously, due to losses throughout the system, this value is not the same at other locations where measurements of the aerosol are taken.

$$\alpha_{ext} = \frac{R_L}{c_{air}}\left(\frac{1}{\tau} - \frac{1}{\tau_0}\right) = \sigma_{ext} N_{CRD} \tag{17}$$

This method has a huge advantage over other methods when calculating extinction due to the large effective distances that can be achieved through proper alignment of the laser with the cavity. This gives a high resolution as the laser passes through the aerosol multiple times before it decays to 1/e of its original value. Our maximum ring down time was measured at 80 μs. Given that light can travel at $3 \times 10^8$ m/s, our effective distance is approximately 24 km. Since the length of our cavity is 170 cm, this gives over 140,000 passes for one pulse of the laser. Another advantage of this method is that the resulting measurements are not dependent on pulse-to-pulse variations of the laser intensity—each individual measurement simply measures the time taken to reach 1/e of the initial intensity for that particular pulse.

## 2.6 Integrating Nephelometry

The method used to calculate the scattering coefficients of aerosols is integrating nephelometry (Anderson et al. 1996, Anderson and Ogren, 1998). In order to calculate the absorption coefficients, we will use the extinction-minus-scattering method. Nephelometry is very sensitive due to the fact that scattering (in small quantities) is easier to detect than the resulting attenuation of light caused by the same amount of scattering. As the nephelometer is a common instrument for measuring the scattering of aerosols, only a brief explanation will be given here.

The nephelometer is capable of measuring scattering over a range of angles (compared to the incident light) within its sampling volume. These measurements are made by three photomultiplier tubes (PMTs). Each of these PMTs is paired with a different dichroic filter having one of the following specific wavelengths: 450, 550, and 700 nm. These three measurements can be extrapolated to cover the full visible spectrum using the Ångstrom coefficient mentioned in the first chapter. Previous work was done to determine the uncertainty contributed by the nephelometer (Massoli et al. 2009, Singh et al. 2014). It was found that a correction factor needed to be applied to match the scattering coefficient with the extinction coefficient for purely scattering particles. This will be discussed in the fourth chapter.

## 2.7 Summary

As mentioned above, the soot particles that we are interested in have a size of 100 to 700 nm. We are investigating their optical properties in the visible spectrum, which ranges from about 400 to 700 nm. Since these are on the same order of magnitude, we must use Mie theory to determine their properties, without relying on the Rayleigh approximation. Since Mie theory only works for spherical particles, it can be applied to manufactured spherical aerosols in order

to calibrate our system. These will serve as an upper limit when considering the equal-volume-size parameter $X$ of our non-spherical particles.

# CHAPTER 3

## Experimental Details

### 3.1 Soot Aerosol Collection

Soot aerosol is generated by burning biomass in the form of wood. Wood was placed in a fifty-five gallon steel barrel (Figure 3). A hood and chimney was made using an aluminum bucket with a galvanized steel pipe attached. The steel barrel had holes drilled in the side to allow air flow. This flow could be adjusted by sliding a sheet of aluminum around the barrel to block or unblock the holes. However, it was found that the fire was being smothered unless more air was allowed to enter the drum through the gap between the barrel and the hood. While most of the soot escaped through this gap or the chimney, part of it was drawn through half-inch copper tubing connected to the side of the chimney. This was coiled to act as a passively-cooled heat exchanger. Care had to be taken not to let the copper tubing rest above the fire as this would not allow the soot to cool down. The coil was set at an angle to allow any condensation to drip back into the fire. This was then connected to half-inch Teflon tubing, which ran to a junction. Quarter-inch tubing was used initially, but it was found that larger tubing was needed to prevent it from getting clogged with condensation. From there, the soot was split into three flows: one for soot collection via impinger, one for soot collection via cascade impactor, and one for size distribution analysis via scanning mobility particle sizer (SMPS).

An impinger (Ace Glass, model 7542-06) was used to collect the soot for analysis in the laboratory. Chloronapthalene was originally chosen for its compatibility with soot; however, this solvent was found to cause problems with the aerosol generation equipment in the lab. Instead, distilled water was used as a solvent. Although not all of the aerosol particles were captured, we were still able to study those that were water-soluble. The impinger was filled with 30 mL of

distilled water, with a flow rate of 12.5 L/min as specified in the catalog for use with this type of impinger. This flow was maintained by a vacuum pump (Gast, model DOA-P701-DB) which served as the main method to draw the soot from the chimney. Each sample was taken for 15 minutes. The impinger was then emptied into sample jars using disposable pipettes. Care was taken not to transfer large (visible) pieces of soot into the sample jars, since they were obviously beyond the size range of interest for this study.

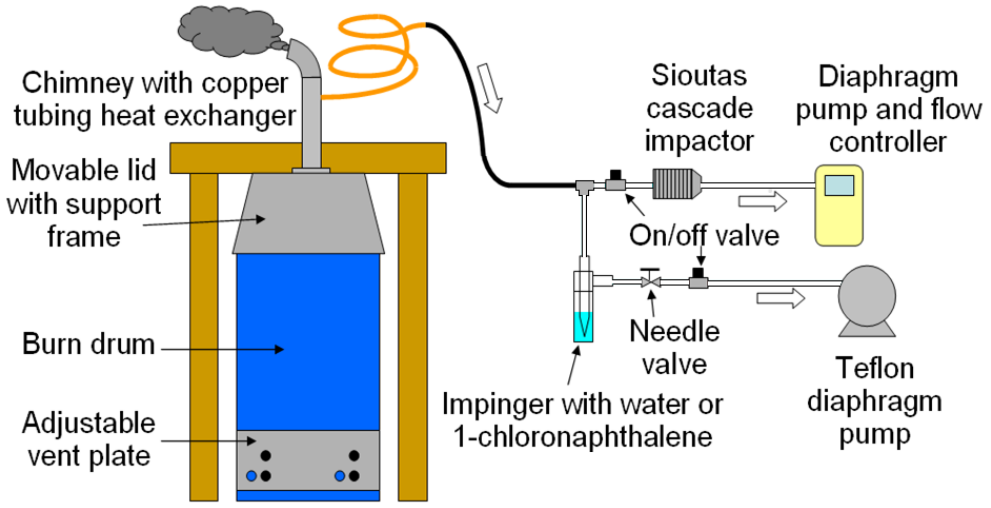


*Figure 3.* Soot aerosol collection system.

A Sioutas cascade impactor was used with a Leleand Legacy pump (both obtained through SKC) to collect the soot on filters to be analyzed by a scanning electron microscope (SEM). This was done at the microscopy lab at the Joint School of Nanoscience and Nanoengineering. The samples were collected on aluminum filters, which were selected based on their conductivity. The impactor also contained a Teflon filter. Samples were collected for 3 minutes. For times much longer than this, the pump on the impactor began to choke and our samples became saturated. The filters were then removed from the impactor and stored in Ziplock bags. The particle size cut-points for the impactor are 2.5 µm, 1.0 µm, 0.50 µm, and 0.25 µm. Only the smallest size range was actually viewed under the SEM because the others were

beyond the range of interest for this study. The SEM was used to determine the general size and shape of the soot particles. Figure (4) shows the fractal nature of one of the samples.

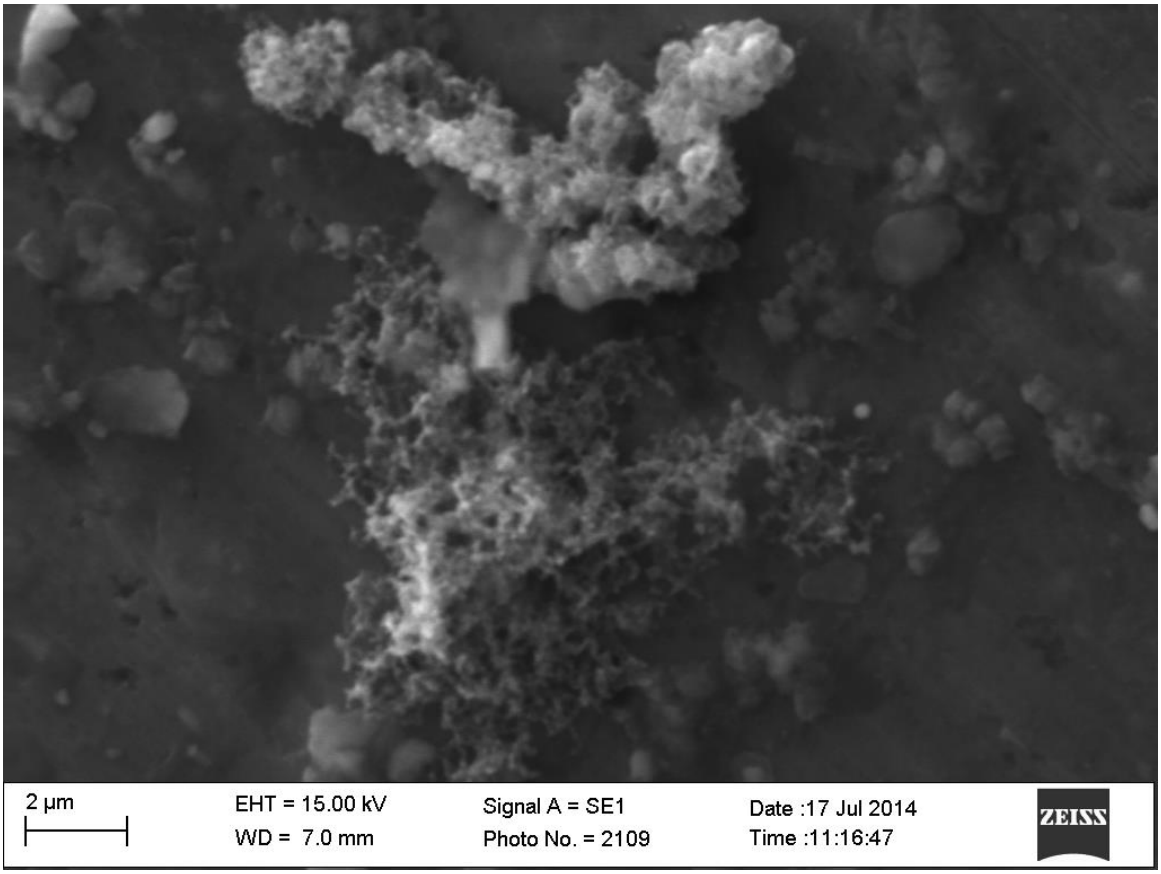


*Figure 4.* Scanning electron microscope image of soot aerosols during the flaming stage.

A scanning mobility particle sizer (SMPS) was used to determine the size distribution of the aerosol generated. This was later compared to size distributions of the soot after being re-aerosolized in the laboratory. The morphology of the soot will change after it has been put into a solution due to chemical interactions. Soot also becomes more compact as it ages (Zhang et al. 2008). This would mean that the optical properties measured were not representative of fresh soot. Unfortunately, not much was gained from this measurement since it exceeded the maximum capabilities of our SMPS, which will be described in more detail in the laboratory setup.

Soot samples were taken during each stage of burning: ignition, flaming, and smoldering. The ignition stage was contaminated with particles from the method used to start the fire: cardboard, gas, etc. These samples were not analyzed in the lab. Care had to be taken not to smother the fire during the flaming stage; otherwise, the smoldering stage was entered prematurely. Soot samples were also taken from three different types of trees: white pine, red oak, and cedar. It is uncertain whether the optical properties will vary from one species to another.

### 3.2 Laboratory Setup

**3.2.1 Aerosol Generation.** Once the aerosol had been collected, it was taken to the laboratory for measurement. There, the samples were diluted by adding another 100 mL of distilled water. This ensured that the SMPS would not become maxed out as it was in the field. Before measuring the optical properties of the collected soot, it had to be re-aerosolized (Figure 5).

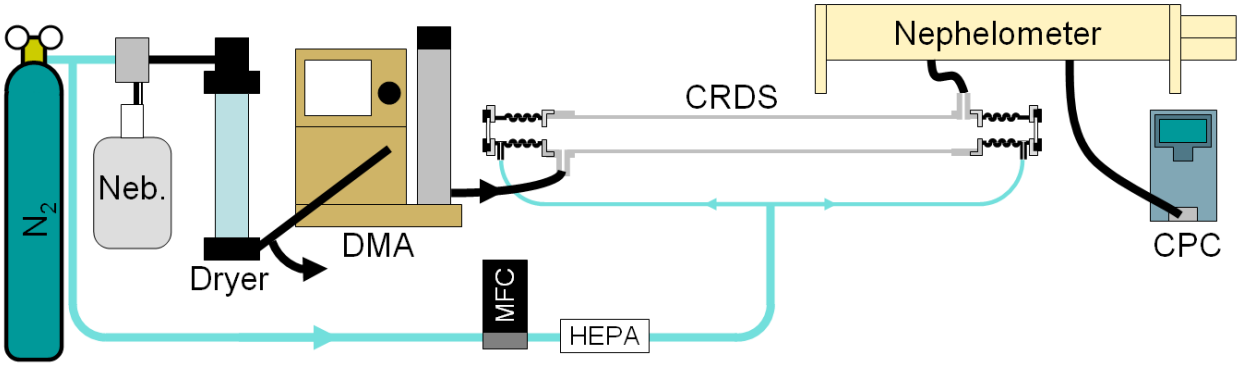


*Figure 5.* Aerosol generation setup in laboratory.

The sample jars were connected to a Model 9302 Single-jet Atomizer and a Model 3062 Diffusion Dryer, both from TSI. The atomizer had a flow of 35 psi of nitrogen, which provided flow throughout the system. The dryer contained silica gel, which removed excess water from the soot particles, effectively turning them back into an aerosol. From here, the particles passed

through an impactor with a cutoff of .0701 cm, which removed any particles that were too big for this study, before going into a Model 3080 Electrostatic Classifier with a Model 3081 Long Differential Mobility Analyzer (DMA), both from TSI. Once inside the classifier, the particles were given a charge. The DMA then used the electric mobility of the particles to choose a specific size to send through the rest of the system.

At this point, the particles entered the cavity, which was made of stainless steel, having a length of 170 cm and an outer diameter of half an inch. The interaction between the aerosol and the laser will be described in the next section. A purge flow of 20 mL/min of nitrogen was used to keep the particles from building up on the highly reflective mirrors at the ends of the cavity. From here, the particles went into a Model 3563 Integrating Nephelometer from TSI. Routine calibration of the nephelometer was generally done before a major round of experiments. Finally, the particles were counted by a Model 3787 General Purpose Water-based Condensation Particle Counter (WCPC).

**3.2.2 Laser and Optics.** To simulate different wavelengths of light, an optical parametric oscillator (OPO) was used, having a bandwidth of ~0.9 nm at 550 nm, ~2 nm at 600 nm, and ~9 nm at 680 nm. The OPO contains a birefringent crystal capable of producing light at wavelengths from the visible range up to the near infrared. The 355 nm beam from a Continuum Surelite I-20 Nd:YAG laser, operated at 20 Hz, was used to pump the OPO. An ND 6000 dye laser is also part of this setup, but was not used to collect data for this study due to technical issues.

Careful alignment of the laser must be used to obtain mode matching within the cavity. Several optical components (Figure 6) were used for this alignment of the beam with the cavity. For the OPO, an iris and achromatic lens with a focal length of 40 cm (Thorlabs, AC254-400-A-ML) were needed to collimate the beam before reaching the other optics. To allow space for both

of the lasers on the optics bench, two silver turning mirrors were used to align the beam from the OPO with the rest of the optics. The following optical setup applies to both of the lasers.

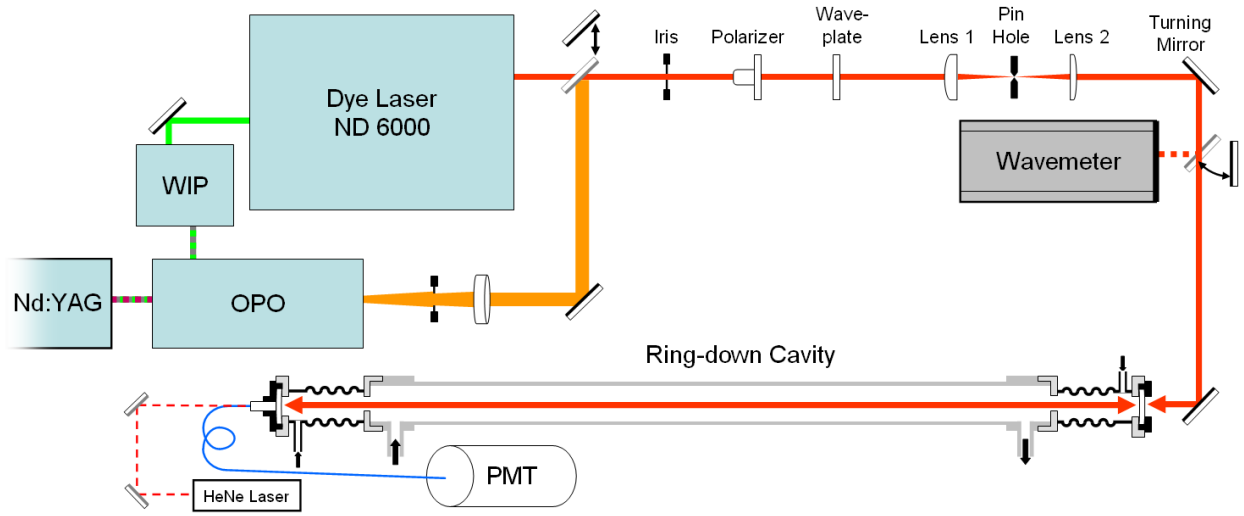


*Figure 6.* Laser and optics setup in laboratory.

An iris was used to block out any parasitics. This gave us a nice round beam to work with. This was followed by a polarizer (Thorlabs, model GL5), which was aligned to allow maximum intensity of the beam to pass through. This was determined by rotating the fast axis of the polarizer until none of the beam could be seen, then rotating it back 90°. A quarter wave plate (Thorlabs, AQWP05M) was then used with its fast axis at an angle of 45° with respect to the fast axis of the polarizer. This kept any reflections from the rest of the system, specifically the highly reflective mirrors, from going backwards into the laser. If the beam is polarized horizontally, a shift of 45° while going forwards and another shift of 45° while going backwards gives a total shift of 90° when compared to the polarizer. This shift in polarization is then canceled by the polarizer.

Next we have a Galilean telescope consisting of two plano-convex lenses having focal lengths of 30 cm and 15 cm (CVI/Melles Griot, PLCX-C series). Both lenses were mounted on moving platforms so that the distances could be adjusted to mode-match with the cavity. This

was primarily done by moving the second lens so that the new focal point of the laser was in the center of the cavity. A pinhole was placed at the focal point to ensure that there were no extra fringes at the beam waist. The pinhole was chosen based on the diffraction limited spot size of the laser beam and is given in equation (18), where *D* is the diameter of the pinhole, $\lambda$ the wavelength of the laser, *f* the focal length of the converging lens, and *r* the radius of the beam waist. Using the upper end of our wavelength spectrum, $\lambda$ was set equal to 750 nm, and *r* was measured to be 3 mm. This gives a pinhole diameter of 87.5 μm. It was found experimentally that a diameter of about twice this value eliminated the diffraction pattern seen from the pinhole itself. The pinhole that was actually used had a diameter of 150 μm. After the laser passed through the telescope, it was cleaned up, reduced by a factor of 2:1, and mode-matched with the cavity.

$$D = \frac{\lambda f}{r} \tag{18}$$

Two more turning mirrors (CVI/Melles Griot, TLM1 series) were used to align the beam with the cavity. Another iris was used between these mirrors for calibration purposes. Throughout the alignment process, a helium neon laser was used going backwards through the cavity to center all of the optics and align the incoming laser beam with the cavity. Once the laser has been aligned with the cavity, the highly reflective mirrors were attached to the ends of the cavity one at a time and aligned with the beam. After this, a photomultiplier tube (PMT) (Electron Tubes Ltd., 9558B) was attached to the far end of the cavity using a fiber optic cable (Thorlabs, M25L01) and collimator (Thorlabs F220SMA-A or F220SMA-B).

### 3.3 Data Collection

Several quantities were measured for each sample. The first was a size distribution of the sample. This was done using the DMA and WCPC in tandem to create a scanning mobility

particle sizer (SMPS). The DMA scans through a range of particle sizes while the WCPC counts the number of particles at each size. This information can then be used to select which size of sample particles to work with. A sample size distribution for soot aerosol is given in Figure (7). This size distribution is Gaussian if the x-axis has a log scale.

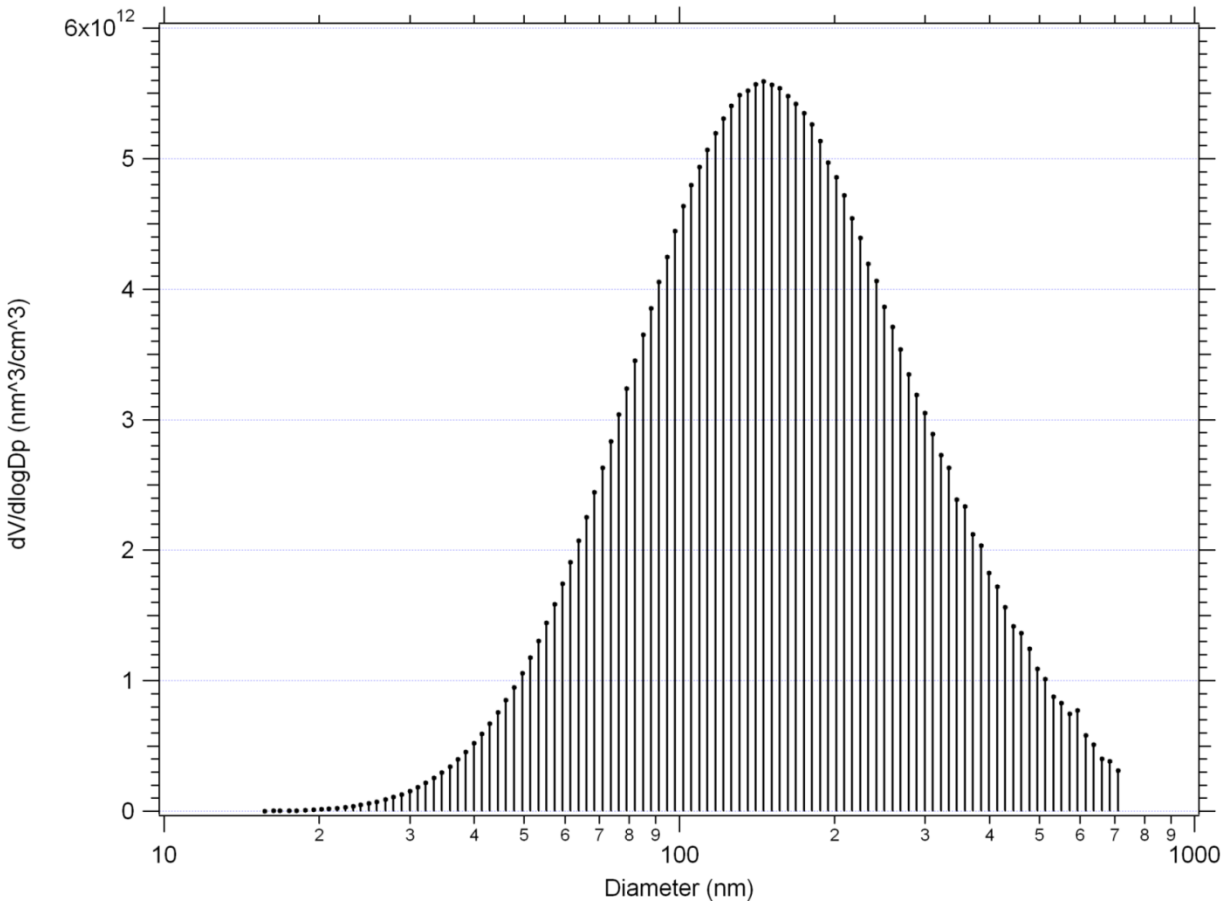


*Figure 7.* Size distribution for soot aerosol. Range of SMPS is approximately 15 to 725 nm.

The PMT was connected to the cavity using a fiber optic cable was used to measure the intensity of light "leaking out" of the cavity. The sensitivity of the PMT could be adjusted using a high voltage power supply. This was measured and plotted by a LabView program as an exponential decay, while measuring the time taken for the intensity to decrease to $1/e$ of the original intensity. This time is called the ring-down time and assigned to the variable $\tau$. $\tau_0$ is the ring-down time with no particles inside the cavity (other than air particles, which cannot be

completely removed). The difference in these values can be used with the geometry of the cavity to find the extinction coefficient as given in the second chapter.

The nephelometer was used to measure the scattering coefficient of the aerosol at predefined wavelengths: red (700 nm), green (550 nm), and blue (450 nm). The values obtained were averages over the length of the experiment. These values can be extrapolated to predict the scattering coefficient at any wavelength of light using the Angstrom Coefficient. Initially, the extinction coefficient and scattering coefficient did not match for perfectly scattering polystyrene latex (PSL) spheres, so a correction factor was applied to reconcile these differences. This correction factor had to be done at each particle size measured to avoid errors caused by extrapolation.

The WCPC counted the total number of particles exiting the system to get the particle number density of the aerosol. Using the data from our loss measurements (described in the next chapter), it can be determined how many particles were inside both of the major components of our system: cavity and nephelometer. These values were used to determine the extinction and scattering coefficients, respectively. From here, the single scattering albedo and Angstrom coefficients could also be found.

# CHAPTER 4

## Results and Discussion

### 4.1 Calibration and Loss Measurements

Calibration of the laboratory equipment was done using manufactured polystyrene latex (PSL) spheres with a known refractive index. Both purely scattering and purely absorbing spheres were used. The size range of the purely scattering spheres was between 100 nm and 700 nm in increments of 100 nm. A size of 400 nm was used for the absorbing spheres due to their availability. It was experimentally determined using our SMPS that the peak concentration of particles were generally larger than the size listed on the bottle from the manufacturer. This may be due to the sensitivity of the SMPS, however, it is more likely that this was caused by the presence of surfactant on the PSL spheres. While the surfactant keeps the PSL spheres from sticking to each other in a solution, it also adds a few nanometers to the thickness of the spheres, which is measured as a larger diameter. Both the manufactured diameter and the experimental diameter are given in Table (1) with particle concentrations in the middle three columns and the loss terms in the last two.

The loss measurements themselves were taken at three points in the experimental setup: before the cavity, after the cavity, and after the nephelometer. The WCPC was used to measure the concentration of the aerosol at each of these points. A 10-inch piece of tubing with a connector was used in front of the WCPC for all measurements. The aerosol particles that made it through all of the aerosol generation equipment, up to and including the DMA and the tubing from the DMA to the cavity, were considered as the starting concentration of aerosol. The next measurement included the volume of the cavity. More specifically, the purge flow volume was not included in this measurement. Finally, the nephelometer and all tubing connected to it were

included in the last measurement. These losses were used to calculate error in aerosol concentration within the cavity and nephelometer volumes. Previous work was done using the PSL spheres to study sources of systematic error within our system (Singh et al. 2014) and it is applied in the analysis in this work and briefly discussed here.

Table 1.

*Loss measurements for the cavity and nephelometer.*

| Manufactured Diameter (nm) | Experimental Diameter (nm) | Before CRDS | Before Neph. | After Neph. | $L_{CRD}$ | $L_{Neph}$ |
|---|---|---|---|---|---|---|
| 102 | 105.5 | 4970 | 4650 | 3370 | 0.9356 | 0.7247 |
| 203 | 213 | 1250 | 1220 | 1000 | 0.9760 | 0.8197 |
| 296 | 304 | 386 | 359 | 291 | 0.9301 | 0.8106 |
| 390 | 390 (A) | 251 | 227 | 174 | 0.9035 | 0.7675 |
| 400 | 404 | 263 | 244 | 217 | 0.9278 | 0.8893 |
| 498 | 525 | 107 | 97.7 | 80.8 | 0.9157 | 0.8270 |
| 600 | 625 | 86.4 | 78.7 | 65.3 | 0.9109 | 0.8297 |
| 707 | 740 | 18.1 | 17.3 | 14.2 | 0.9558 | 0.8208 |

**4.2 Error Analysis**

A comprehensive treatment of CRDS random and systematic error has been performed by Miles et al. (2011) and our lab (Singh, 2014). The error analysis performed for absorbing and nonabsorbing polystyrene spheres is applied in analyzing the data presented here for soot. The analysis is described below.

In this work, ring-down decays are plotted on a log scale and a least squares linear fit is performed between two user-selected cursors in LabVIEW. In our work it is unlikely that cursor

selection has an important effect compared to run-to-run variability, so long as low S/N is avoided and the ring-down trace cursors are observed to be appropriate over the wavelength range of the experiment.

A potential source of random and systematic error is the difference between the aerosol concentration in the ring-down cell and where it is measured in the WCPC. There are several mechanisms for particle losses in the system, including dilution due to purge flows, gravitational settling, inertial impaction at the inlet, and diffusion to the walls (Pettersson et al. 2004). In this work we have elected to perform WCPC measurements before and after the cavity and nephelometer to determine losses empirically. The loss term $L$ for each instrument (Table 1) is the fraction of particles making it through the instrument ($L$<1). Loss in the nephelometer ($L_N$) is assumed to occur after the sampling volume. For the CRDS, it is assumed that the concentration within the CRDS is (or is, on average) midway between the particle concentration entering and exiting the cavity. Thus the relation between the number density measured at the WCPC ($N_{WCPC}$) can be related to the number density in the cavity ($N_{CRD}$) and in the nephelometer ($N_{Neph}$) by equations (19) through (21). It is possible that, due to optical tweezing effects (Butler et al. 2007), the particle number density within the beam is higher than the bulk; however, these contributions were found to be negligible.

$$N_{Neph} = \frac{N_{WCPC}}{L_{Neph}} \tag{19}$$

$$N_{CRD} = \frac{N_{WCPC}}{2L_{Neph}}\left(\frac{1}{L_{CRD}} + 1\right) \tag{20}$$

$$\frac{N_{CRD}}{N_{Neph}} = \frac{\left(\frac{1}{L_{CRD}}+1\right)}{2} \tag{21}$$

Another factor impacting the accuracy is the potential for coherent forward-scattered light to be recaptured by the resonating pulse of light in the optical cavity (Smith 2011). This results in the observed extinction cross section ($\sigma_{ext,obs}$) being smaller than the actual extinction cross section because a portion of the scattered light is not removed from the beam, and is instead coupled back into the incident beam. In that work, an upper bound in the relative extinction cross section change was found to be given by equation (22), where $\omega_0$ is the beam waist radius (the denominator being the beam diameter) and $V$ is the laser beam volume. While this volume was assumed to be cylindrical in this theoretical work ($\pi\omega_0^2 d / R_L$), this likely underestimated the number of particles within the beam ($N_{CRD}V$), since the beam is wider at either end of the cavity. The systematic correction due to recapturing forward-scattering light is extremely small relative to other sources of random and systematic error, and therefore, correction due to this effect is neglected in this work.

$$\left|\frac{\Delta\sigma_{ext}}{\sigma_{ext}}\right| < N_{CRD}V\left(\frac{D_p}{2\omega_0}\right)^3 \approx \frac{\pi d}{4R_L}N_{CRD}{D_p}^2 \tag{22}$$

It is assumed that $\tau$ and $\tau_0$ are normally distributed and not correlated. If instrument error is associated with $\tau_0$ and any differences between the standard deviations, $s(\tau)$ and $s(\tau_0)$, are due to statistical fluctuations in the particle concentration, it can be assumed that $s(\tau) = s(\tau_0)$ and that the instrument and particle statistics errors are additive and separable. The standard deviation of the extinction cross section $s(\sigma_{ext})$ is given by equation (23). While it may appear that this equation fails when $\tau = \tau_0$, it does not when $\alpha$, which has $\tau$ and $\tau_0$ terms in it, is multiplied through it.

$$s(\alpha_{ext}) = \alpha_{ext}\sqrt{\frac{1}{N_{CRD}Vrt_s} + \left(\frac{s(R_L)}{R_L}\right)^2 + \frac{s(\tau_0)^2}{(\tau-\tau_0)^2}\left(\frac{{\tau_0}^2}{\tau^2} + \frac{\tau^2}{{\tau_0}^2}\right)} \tag{23}$$

Using error propagation methods, the standard deviation of the extinction cross section $s(\sigma_{ext})$ is given in equation (24). For any correction to the number density that doesn't contribute to the error, it can be shown that RSD of the WCPC (0.1) can be directly applied to the CRDS without alteration.

$$s(\sigma_{ext}) = \sigma_{ext}\sqrt{\left(\frac{s(N_{WCPC})}{N_{WCPC}}\right)^2 + \frac{1}{N_{CRD}Vrt_s} + \left(\frac{s(R_L)}{R_L}\right)^2 + \frac{s(\tau_0)^2}{(\tau-\tau_0)^2}\left(\frac{{\tau_0}^2}{\tau^2} + \frac{\tau^2}{{\tau_0}^2}\right)} \quad (24)$$

The largest contributor to the errors is easily the uncertainty of the WCPC, followed by $s(\tau_0)$. Changes of $s(\alpha)_{stat}$ mostly reflects concentration variations on different days, not between runs on the same day. In comparing the overall % error to the error when contributions are removed, the removal of the particle statistics contribution makes an insignificant difference under these conditions and $R_L$ only produces a change of ~0.03 percentile points. Without the contribution of WCPC error, the overall error drops between 8.9 percentile points on the low end of error and only 5.2 in cases where the $s(\tau_0)$ dominates. The wavelength variability is only attributed to $s(\tau_0)$, and the overall error becomes 10.03% uniformly and seemingly without significant contribution from either $s(\alpha)_{stat}$ or $R_L$.

There are a number of other contributors to the uncertainty of the nephelometer. After calibration with reference gases and blanking adjustments, most nephelometers must take into account truncation errors, non-ideal angular response, imperfect wavelength response, and aerosol sampling issues (Anderson et al. 1996; Müller et al. 2009). For backscattering measurements, the shutter does not provide a perfectly sharp separation at 90° (Anderson et al. 1996). The systematic error due to non-idealities is strongly dependent on particle size and is more significant for particles >1 μm in diameter (Müller et al. 2009) due to the forward truncation angle cutoff altering measurements of these strongly forward-scattering particles. Sub-micron particles are more prone to errors resulting from non-Lambertian illumination. Below 50

nm, the accuracy of the nephelometer is only dependent on the accuracy of the calibration gas and photon-counting statistics, because scattered light is radiated isotropically (Anderson et al. 1996). For the nephelometer used here, the precision is excellent, and is generally ~1%. This instrument mainly suffers from the inability to measure strongly forward (>170°) or backward (<~7°) scattered light, non-idealities in the cosine-weighted diffusing lens that follows the light source (because Lambertian (isotropic) illumination over all angles is imperfect), and detector band width (Anderson et al. 1996; Anderson and Ogren 1998).

Several corrections were performed to nephelometer measurements. Particle loss measurements within the nephelometer, performed similarly to the CRD cell, revealed significant losses at these flow rates. These were performed with the manufacturer-supplied bypass block in place, and losses were significantly greater when the unpowered blower was in place. The bypass block or blower is mounted after the scattering volume. The losses were significantly greater than the manufacturer's specified losses (<5%). To take these losses into account, it was initially assumed that particles were lost after the sampling volume, as opposed to before or within. This makes the concentration of particles within the nephelometer $N_{Neph} = N_{WCPC}/L_N$.

A broadband correction factor $A$ was used to reconcile scattering with extinction for completely scattering particles. This also enabled the determination of whether or not to apply the empirical Ångstrom exponent-based correction of Anderson and Ogren (1998) to each channel of the nephelometer. The determination of the corrected scattering coefficient $\alpha_{scat}$ uses equation (25), where $C(\lambda)$ is a truncation angle correction factor, which could be the Anderson and Ogren correction, or some other user defined correction.

$$\alpha_{scat}(\lambda) = AC(\lambda)\alpha_{scat,uncor}(\lambda) \quad (25)$$

Uncorrected scattering cross sections were found to be smaller than extinction cross sections. For completely scattering particles, values for extinction and scattering should be equal (i.e. have a single scattering albedo (SSA) of 1). Since this CRDS system is well-characterized and is an absolute measurement, a broadband (i.e. applied to all channels) correction factor for the nephelometer was found for each particle size and mirror set used here. By plotting the mean extinction cross section vs. the mean scattering cross section and performing a forced-through-zero linear fit, the correction factor *A* can be found by the inverse of the slope. A possible cause for the necessity of using *A* would be if particles were lost within or before the measurement volume of the nephelometer. Since cross sections found using the nephelometer were systematically smaller than the CRDS, this would make sense.

Several works point to a required accuracy for SSA when used in radiative transfer models. While Mishchenko et al. (2004) suggested an SSA accuracy of 0.03, Bond et al. (2009) argue that an accuracy of 0.02 is required. Given that SSA is limited to values ≤1, an accuracy of ≤2% is extremely challenging for a factor that relies on multiple measurement techniques. Previous work using a similar setup estimated SSA uncertainty to be <12% at 532 nm (Li et al. 2011), or variable depending on SSA (Massoli et al. 2009). When determining SSA using equation (3), the number density in the CRDS and nephelometer is included. When propagating the error from this equation, the WCPC error is included twice, which causes SSA errors of 14.5-27.9% for 107 and ~14.3% for 207 and 303 nm PSL particles. A way of improving this would be to use the relationship between the number densities in each instrument instead of using the absolute values for number densities. This results in $N_{CRD}/N_{Neph}$ being replaced with $((1/L_{CRD})+1)/2$ (or *Z* for short), and the error is only dependant on the relative standard deviation (RSD) of $\alpha_{scat}$ and $\alpha_{ext}$. If one assumes this relationship is free from error the SSA error becomes

3.5-32.6% (8.0% average), 1.7-4.1% (2.1% average), and 1.7-4.3% (2.1% average) for 107, 207, and 303 nm particles, respectively. The run-to-run variability of SSA measurements is on par with this. Assuming an error in $C(\lambda)$ can be maintained ≤2% through methods described in above, a mean SSA error of ≤2.9% is expected using this method. Errors of ≤2% is somewhat unreasonable, since even the most complex schemes involving determining $C(\lambda)$ with an assumed refractive index and size distribution information can lead to $C(\lambda)$ error of ≤2% alone. Only through a separate and accurate measurement of refractive index and size distribution can SSA error be further reduced. Yet, compared to previous work with similar setups, these errors are quite low. Massoli et al. (2009) observe nephelometer scattering cross section errors using Anderson and Ogren (A&O) correction to be 3% at SSA = 1, increasing to 5% at SSA = 0.7, and 29% at SSA = 0.4. This is the main contributor to SSA error, which is 30% at SSA = 0.4. They reduced this to 25% using an alternative scheme for deriving $C(\lambda)$, but the CRDS/PAS combination yielded SSA errors of between <1% at SSA = 1 and 8% at SSA = 0.4. This is likely optimistic in light of the CRDS error described in this work. Should a scheme bear fruit, whereby the nephelometer error is reduced by increasing the accuracy of $C(\lambda)$, the CRDS/Nephelometer combination would be more than competitive with CRDS/PAS.

Using the relationship between number densities in the CRDS and nephelometer, the influence of WCPC error on the absorption cross section can also be reduced. The RSD of the absorption cross section is in equation (10), where WCPC error only appears once instead of, effectively, twice. When equation (26) is employed, the absorption cross section error for 390 nm absorbing polystyrene latex (APSL) spheres becomes 11.1-44.3% (mean of 15.1%). While this is large compared to instruments that measure only absorption, it does represent a significant improvement.

$$\frac{s(\sigma_{abs})}{\sigma_{abs}} = \sqrt{\frac{(s(\alpha_{ext})/Z)^2}{(\alpha_{ext}/Z - \alpha_{scat})^2} + \left(\frac{s(N_{WCPC})}{N_{WCPC}}\right)^2} \quad (26)$$

### 4.3 Results

Graphs containing the data gathered during this study are presented at the end of the chapter. All measurements were done with an aerosol particle size of 400 nm, using the OPO with a wavelength range of 515 to 560 nm. Flow rate through the DMA and WCPC was 2.8 L/min and 0.6 L/min respectively. Excess flow is removed from the system before reaching the WCPC. Relative humidity varied slightly, but remained consistent over the time interval of each experimental run, which was between 10 and 20 minutes. Particle number density also varied somewhat over the experiment (generally decreasing), but remained mostly consistent. Any runs where the number density was seen to fluctuate were ignored.

In general, error was higher for smaller wavelengths, due to the range of the highly reflective mirrors being used. This is almost directly caused by decreased ring down time as more light is allowed to pass through the mirrors, leading to a faster loss in intensity of light, resulting in a lower ring down time.

The PSL spheres are plotted in Figure (8). As mentioned previously, a correction factor was applied such that the extinction cross section matches up with the scattering cross section to give an absorbing cross section of zero. This same factor was applied to both the absorbing spheres and the soot aerosol. In general, the cross sections of both aerosol types decreased with respect to wavelength.

In Figures (12) through (14), the cross sections of all aerosols are graphed without error bars to allow comparison without confusion. For the flaming stage of burning, all three types of wood had similar cross sections for both extinction and scattering. The variation between types of wood was 4-7% for the extinction cross section and 6-8% for the scattering cross section. For

the smoldering stage of burning, the variation was much higher, at 10-13.5% for the extinction cross section and 30-40% for the scattering cross section.

The single scattering albedo for all types of wood had a slope close to zero, meaning that this quantity is independent of the wavelength in the range of wavelengths used in this experiment. One interesting thing to point out is that the SSA of the red oak during the smoldering stage was much lower than during the flaming stage, meaning that soot from the smoldering stage is actually more absorbing than during the flaming stage. This is opposite from the other two types of wood studied, as their SSA during the smoldering stage was higher than the flaming stage, meaning the soot is less absorbing.

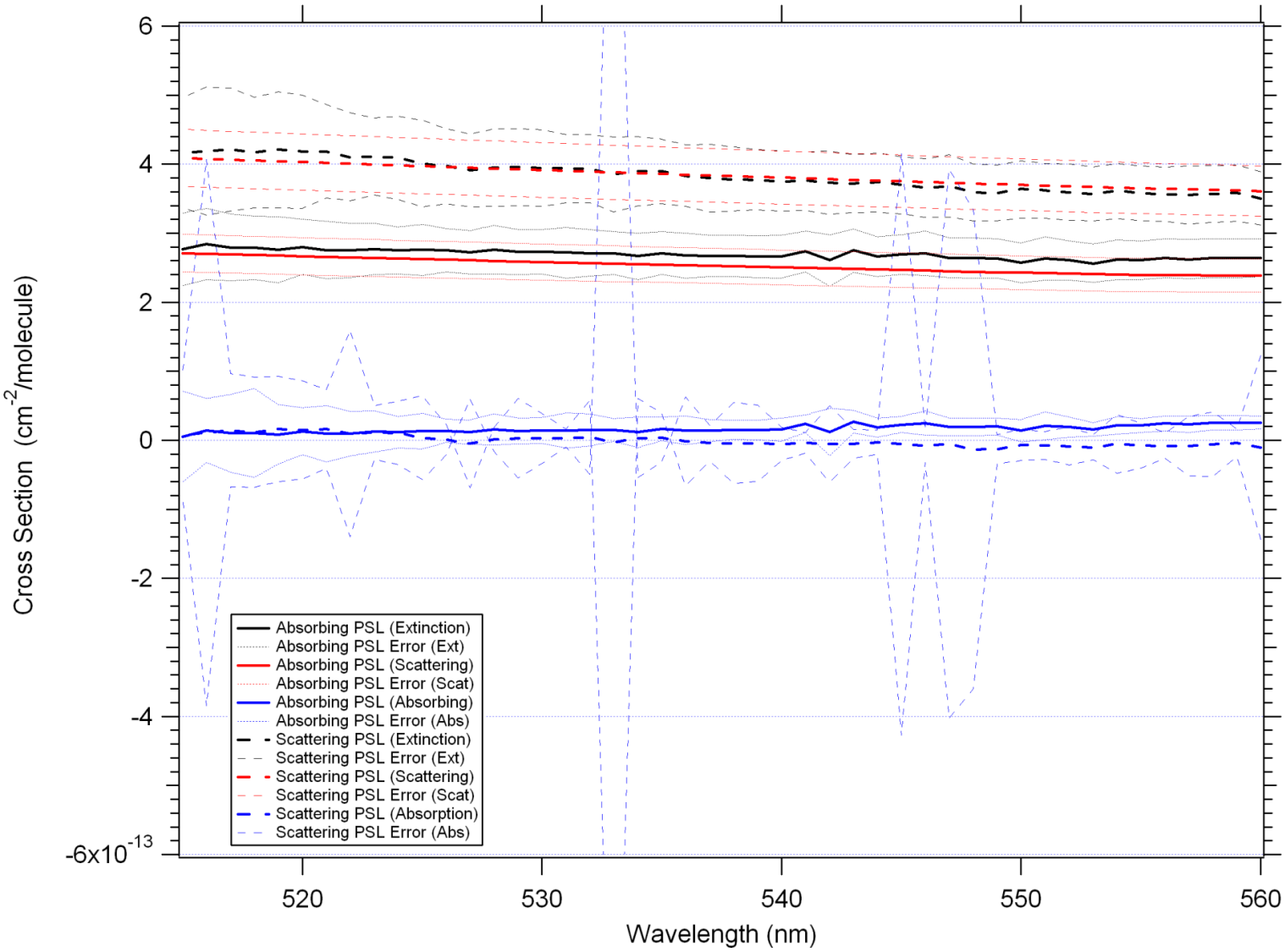


*Figure 8.* Extinction, scattering, and absorption cross sections for scattering and absorbing PSL spheres.

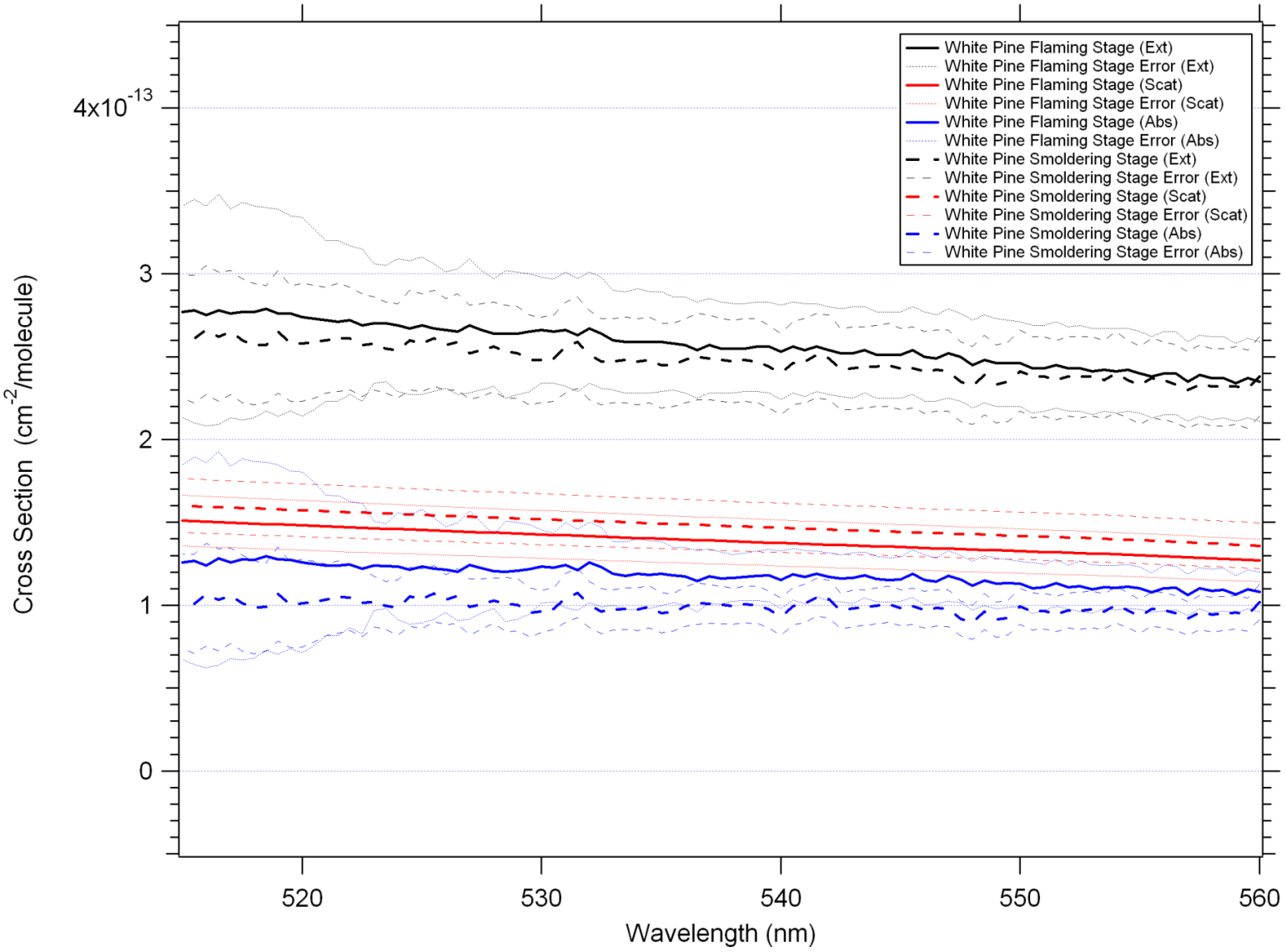


*Figure 9.* Extinction, scattering, and absorption cross sections for white pine during flaming and smoldering stages.

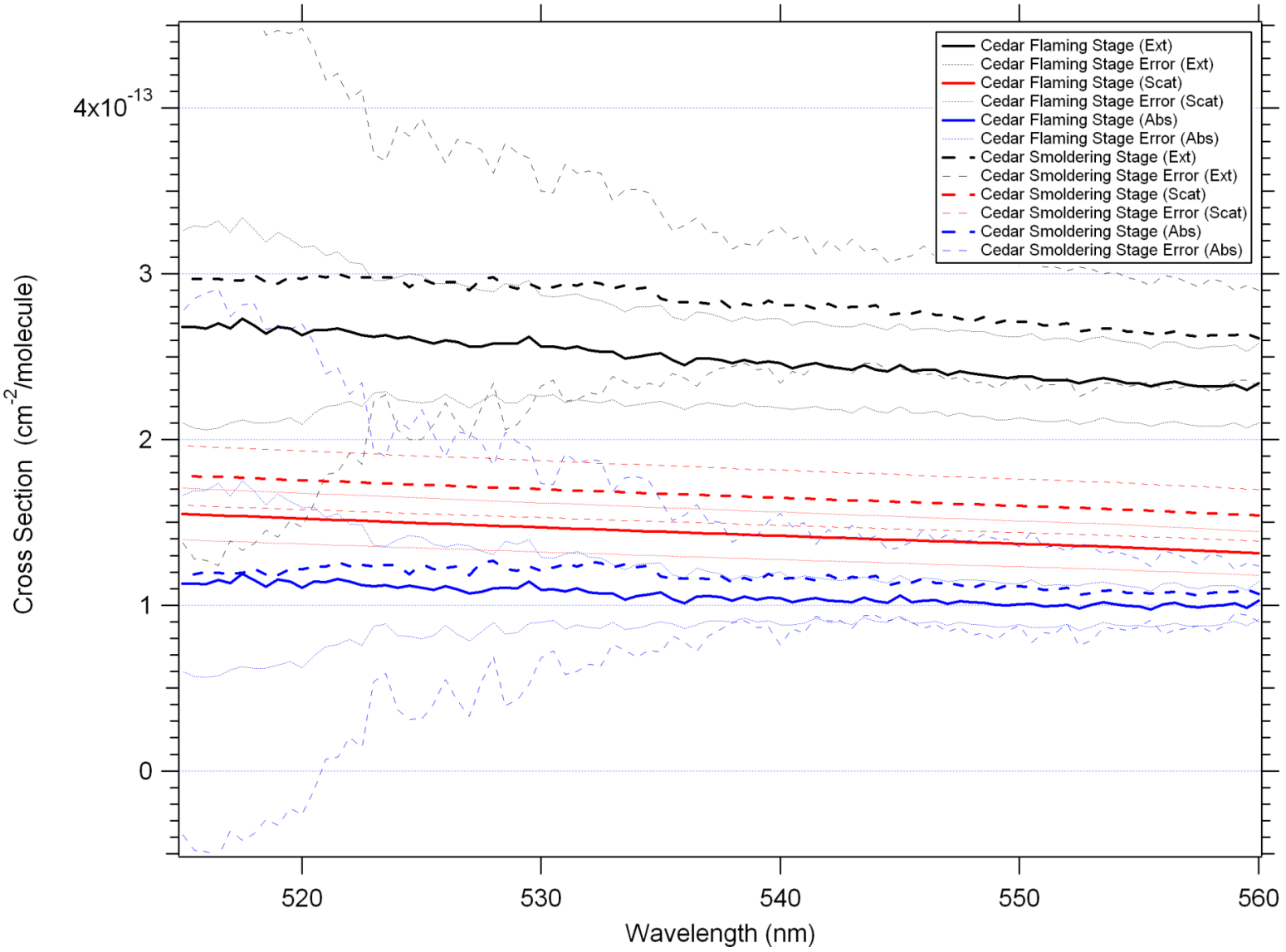


*Figure 10.* Extinction, scattering, and absorption cross sections for cedar during flaming and smoldering stages.

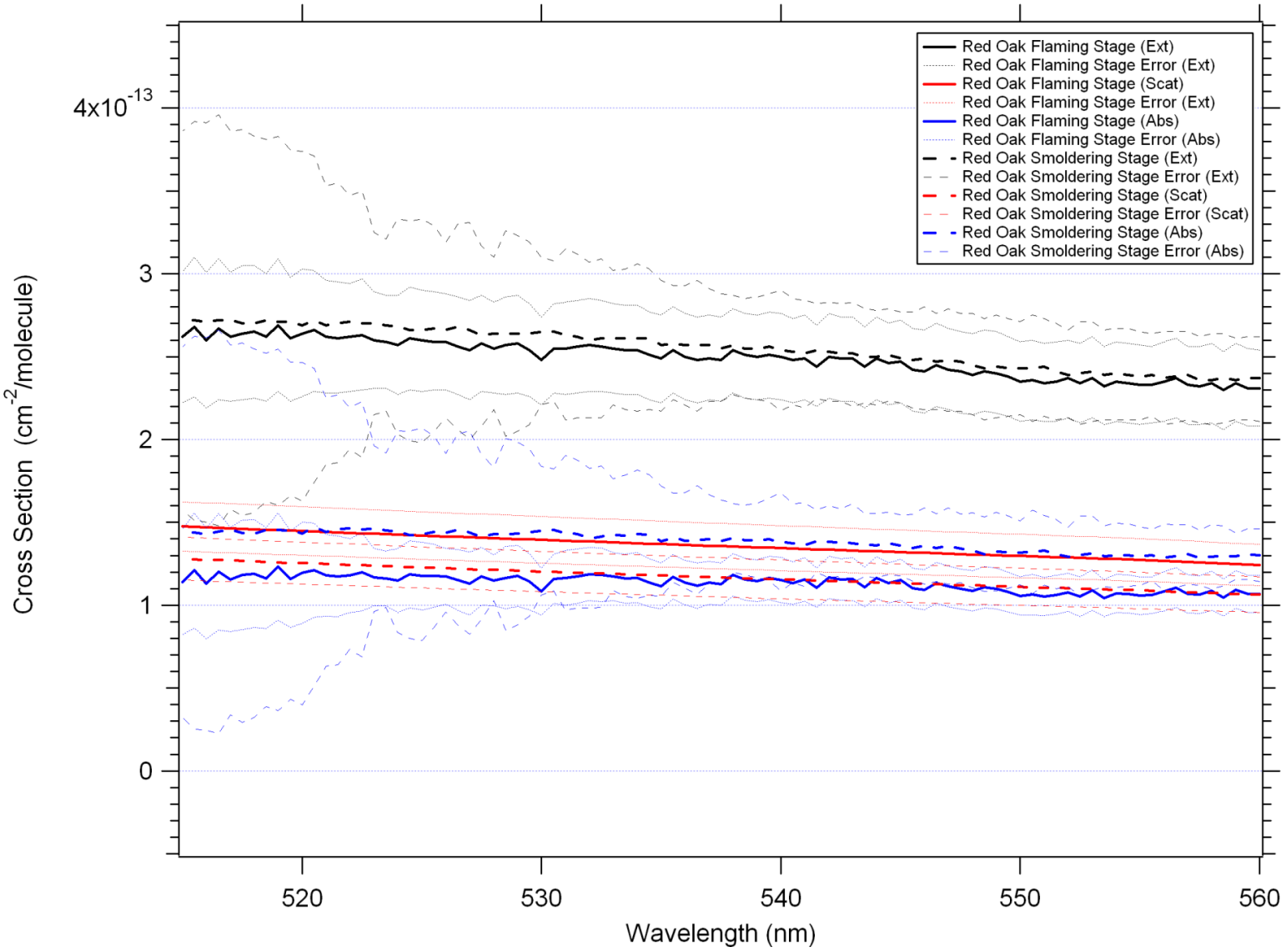


*Figure 11.* Extinction, scattering, and absorption cross sections for red oak during flaming and smoldering stages.

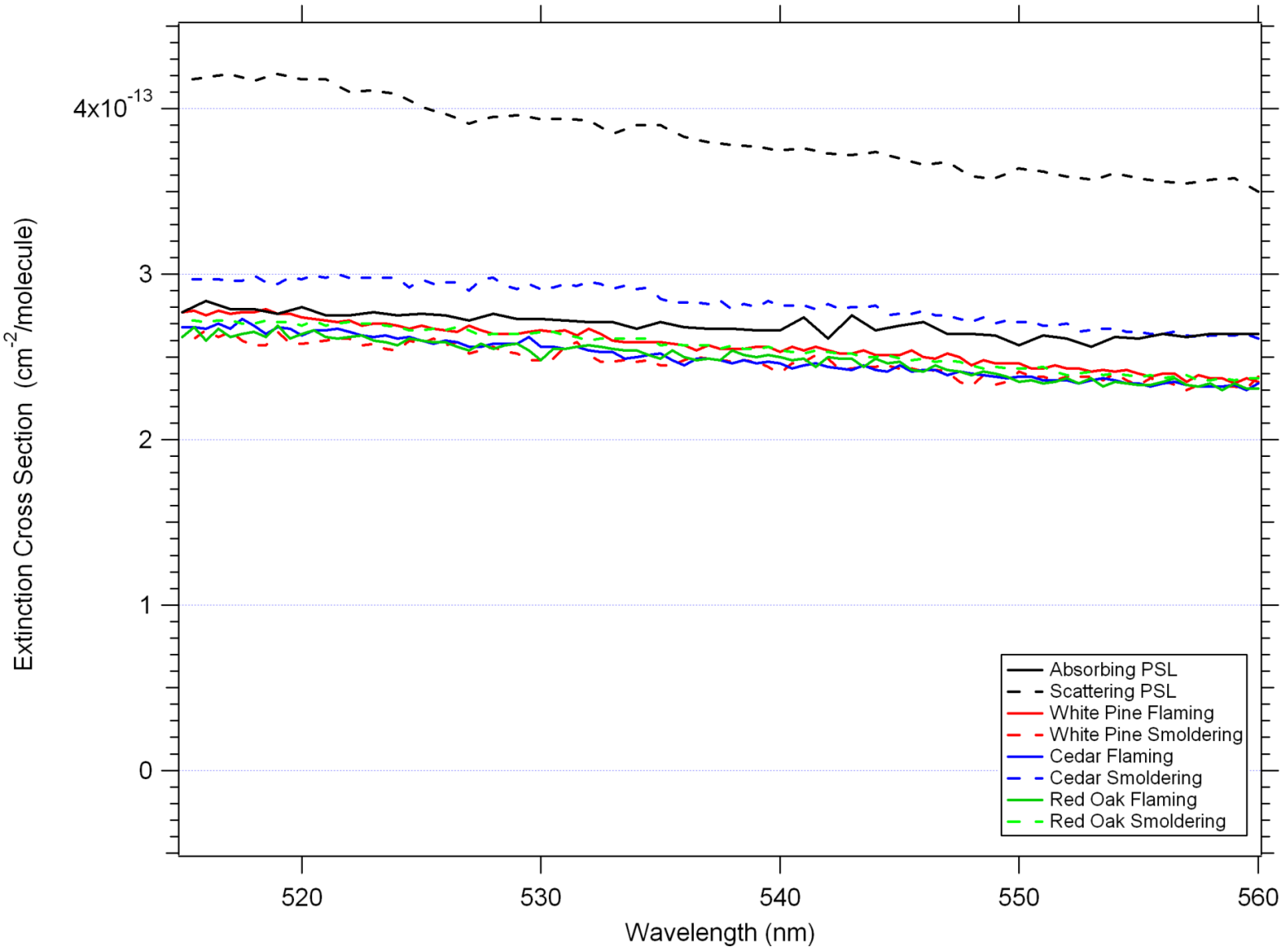


*Figure 12.* Comparison of extinction cross sections among PSL spheres and soot samples. Error bars not included for clarity.

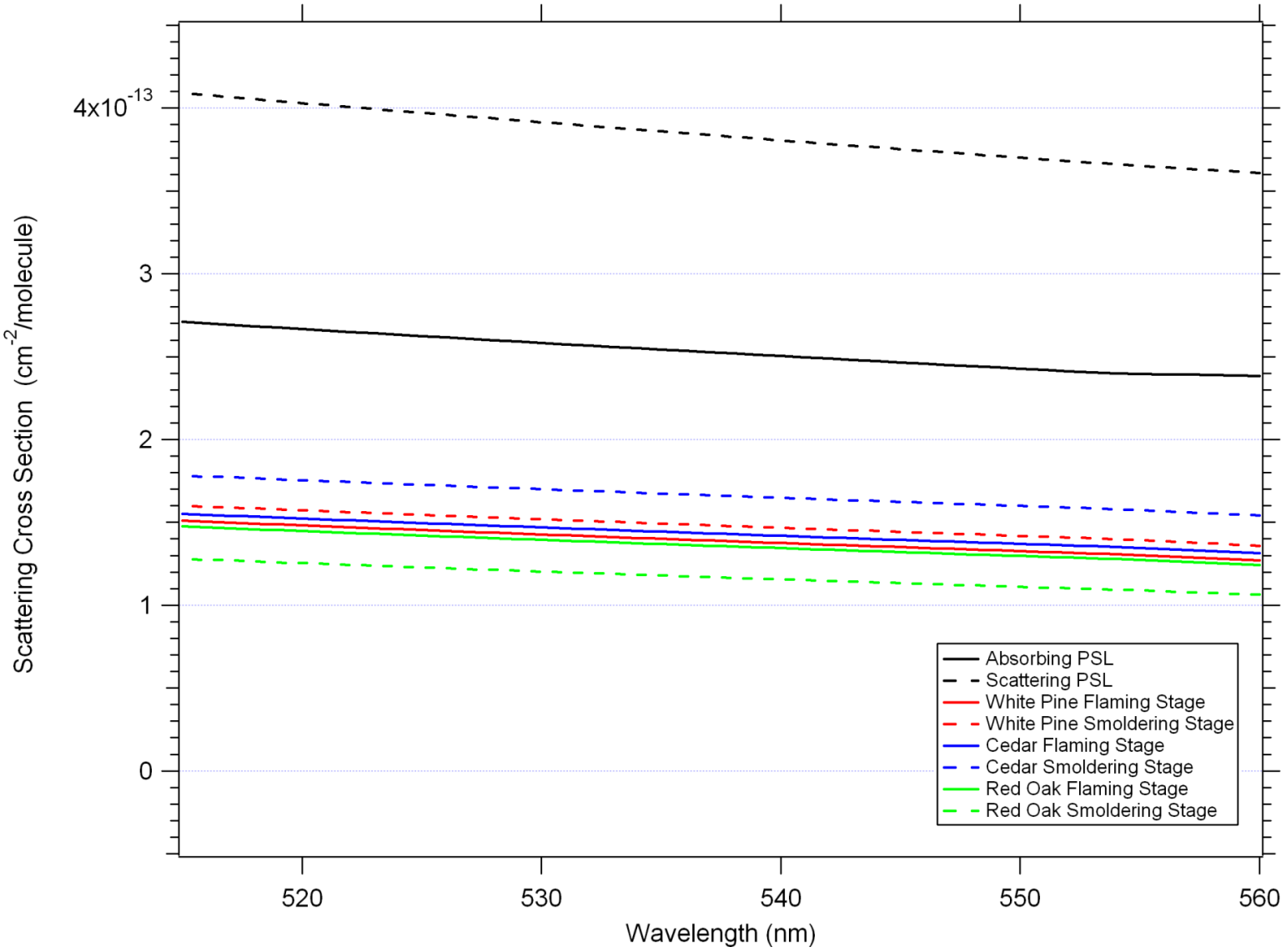


*Figure 13.* Comparison of scattering cross sections among PSL spheres and soot samples. Error bars not included for clarity.

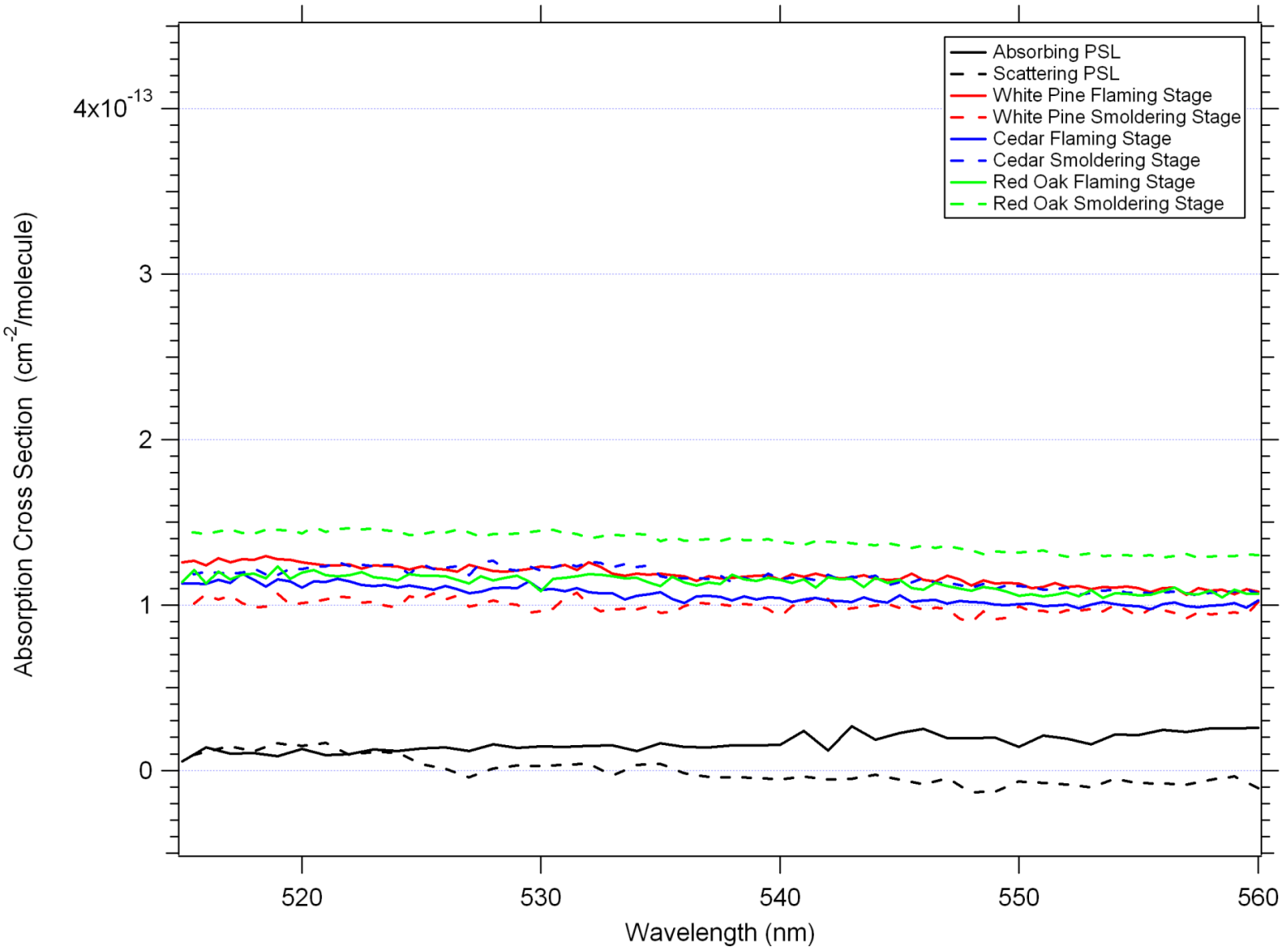


*Figure 14.* Comparison of absorption cross sections among PSL spheres and soot samples. Error bars not included for clarity.

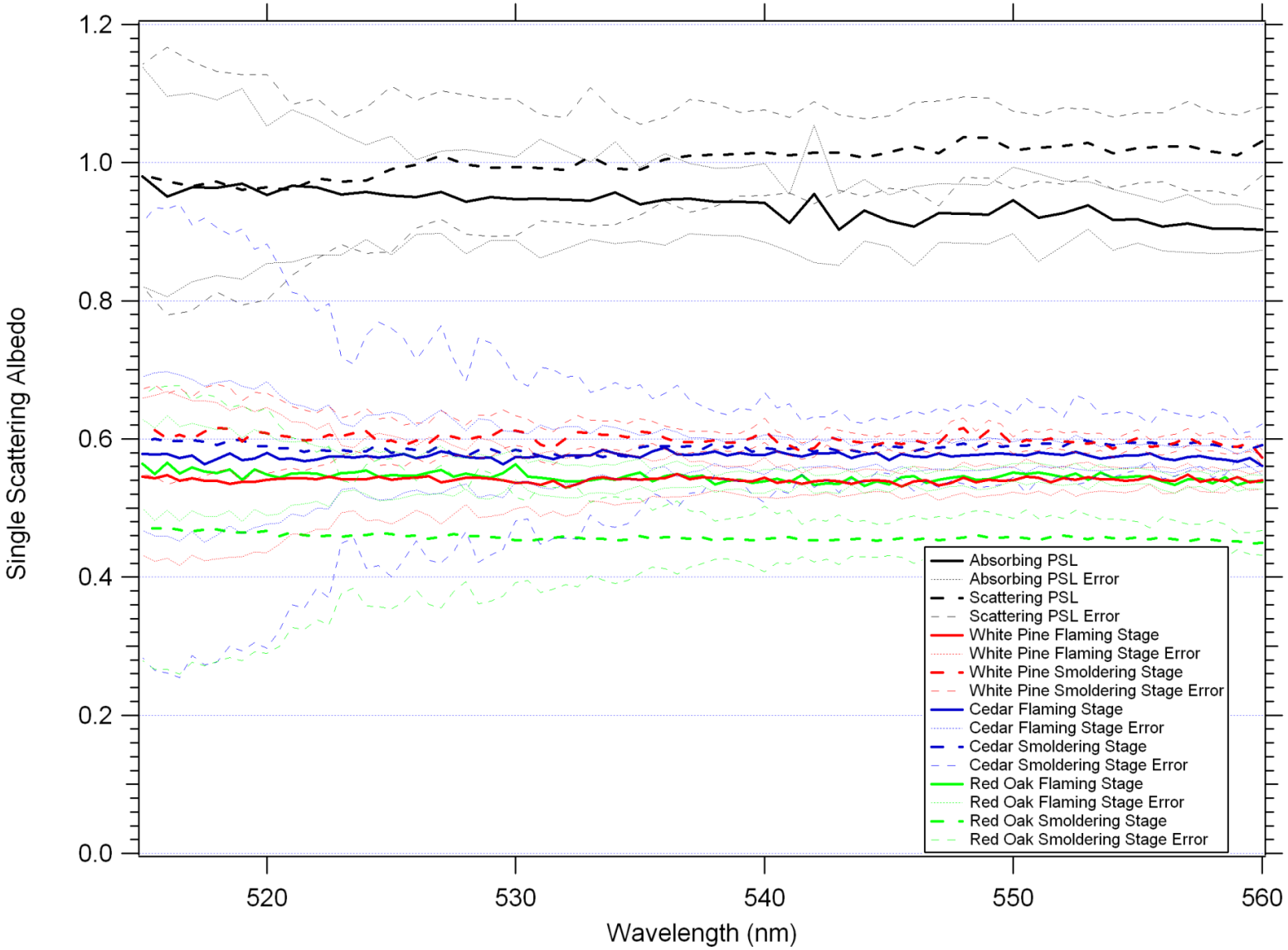


*Figure 15.* Comparison of single scattering albedo for PSL spheres and soot samples.

# CHAPTER 5

## Conclusions

Although we can easily scan through a range of wavelengths using the OPO, we must select one particle diameter at a time to analyze. As previously determined, aerosol sizes <200 nm have greater error and are not recommended for use with our current laboratory setup (Singh et al. 2014). We are also limited by the cutoff of the DMA, which is near 700 nm at the current flow rate of 2.0 L/min. Aerosol particles with a diameter of 400 nm were chosen for this study because both scattering and absorbing PSL spheres were available at this size and correction factors derived from PSL measurements can be applied to the soot samples.

Loss measurements were performed and nephelometer losses were found to be ~17%. Losses in the CRDS were less systematic. We have accounted for all known sources of random and systematic error in a comprehensive and holistic fashion, and have discussed multiple methods for propagating error and sample averaging. A statistical framework was developed for including the contributions to random error due to WCPC measurement uncertainty, ring down cell geometry ($R_L$), statistical fluctuations in particle counts, fluctuations in the blank ring-down time, and MFC flow error. Under the conditions investigated in this work using PSL particles, only WCPC measurement uncertainty and $\tau_0$ fluctuations were significant contributors, though particle statistics may dominate the uncertainty at lower particle concentrations. Systematic uncertainties due to particle losses, $R_L$, WCPC counting efficiency, ring-down regression fitting, $\tau_0$ drift, optical tweezing, and recapturing of forward scattered light were also investigated. For particles in this size range under the cell geometry used here, only the first two factors are important. A broadband correction factor for each particle size and mirror set was found to be necessary to reconcile extinction and scattering measurements for completely scattering

particles, though no wavelength-dependent correction was needed. The employment of correction factors using the method of Anderson and Orgen was evaluated, and was found to be slightly better than a broadband-only correction. Random errors from the correction factors and measurement variability were only slight contributors to $\sigma_{scat}$ error, which was dominated by WCPC error.

By using number density relationships in place of absolute values, the errors in calculated SSA and $\sigma_{ab}$ values could be significantly reduced. Barring significant technological improvements in the accuracy of submicron particle counting, this method is the only foreseeable way of reducing SSA error to acceptable levels. The accuracy of SSA, based on extinction and scattering, is limited largely by the nephelometer at low SSA values. Specifically, the truncation angle correction $C(\lambda)$ is the limiting factor.

The data in the preceding figures only represent a small portion of the visible spectrum, from 515 nm to 560 nm. While we did not observe any significant dependence of the optical properties as a function of wavelength, the range used is too small to rule out any wavelength dependence. Work to measure the properties at a wider range of wavelengths is needed to make such a conclusion. We currently have the ability to increase this range to 740 nm given the capabilities of our OPO and dye laser with our current selection of the highly reflective mirrors.

The high sensitivity of the cavity ring-down system allows for the accurate measurement of extinction cross sections. No observable contribution of water absorption was seen over the wavelengths of light used in this study. Calculating the single scattering albedo (SSA) for a given aerosol allows us to compare different aerosol types to determine which ones are more scattering or more absorbing. This study found that, in general, the SSA for different types of wood during the flaming stage produced values that were much more consistent than during the smoldering

stage (i.e. fuel type does not play a significant role during the flaming stage). The flaming stage, in general, is also more absorbing than the smoldering stage, with the exception of the red oak sample. It is not clear at this time why this is the case. Samples from a wider selection of trees and fuels are needed to determine if the flaming stage is generally more absorbing than the smoldering stage. Cedar was the least absorbing of the three types studied.

Additional types of fuel are also being considered for measurement, including dung and other species of wood. Although our primary focus is soot aerosol, any aerosol could be analyzed using our system, provided it has a size between 200 and 700 nm.

The single scattering albedos found in this work can be used by others to gain a better understanding of how soot aerosols contribute to radiative forcing. By reducing the uncertainty of these measurements, greater accuracy can be achieved for climate models and other applications. Further research will expand upon the work done here, by increasing the wavelength range and studying other sources of soot aerosol.

# References

Ajtai, T., Filep, Á., Schnaiter, M., Linke, C., Vragel, M., Bozóki, Z., Szabó, G., and Leisner, T. (2010). *A novel multi- wavelength photoacoustic spectrometer for the measurement of the UV–vis- NIR spectral absorption coefficient of atmospheric aerosols*, J. Aerosol Sci., 41, 1020–1029.

Anderson, T. L., Covert, D. S., Marshall, S. F., Laucks, M. L., Charlson, R. J., Waggoner, A. P., Ogren, J. A., Caldow, R., Holm, R. L., Quant, F. R., Sem, G. J., Wiedensohler, A., Ahlquist, N. A., Bates, T. S. (1996). *Performance characteristics of a high-sensitivity, three-wavelength, total scatter/backscatter nephelometer*. J. Atmos. Ocean. Technol. 13:967-986.

Anderson, T. L. and Ogren, J. A. (1998). *Determining aerosol radiative properties using the TSI 3563 integrating nephelometer.* Aerosol Sci. Technol. 29:57-69.

Arnott, W. P., Moosmuller, H., Rogers, C. F., Jin, T. F., and Bruch, R. (1999). *Photoacoustic Spectrometer for Measuring Light Absorption by Aerosol: Instrument Description,* Atmos. Environ. 33(17):2845–2852.

Barber, P. W., Hill, S. C. (1990). *Light scattering by particles: Computational methods*. World Scientific Publishing Co.: Teaneck, NJ.

Baynard, T., Pettersson, A., Lovejoy, E. R., Brown, S. S., Lack, D. A., Massoli, P., Osthoff, H., Ciciora, S., Dube, W. P., and Ravishankara, A. R. (2007). *Design and Application of a Pulsed Cavity Ring-Down Aerosol Extinction Spectrometer for Field Measurements*, Aerosol Sci. Technol. 41(4):447–462.

Berden, G., Engeln, R. (2009). *Cavity Ring-Down Spectroscopy: Techniques and Applications*. John Wiley & Sons: West Sussex, UK.

Bohren, C. F.; Huffmann, D. R. (2010). *Absorption and scattering of light by small particles*. New York: Wiley-Interscience. ISBN 3-527-40664-6.

Bond, T. C., Bergstrom, R. (2006). *Light absorption by carbonaceous particles: An investigative review.* Aerosol Science and Technology. *40*. 27-67, DOI: 10.1080/02786820500421521

Bond, T. C., Covert, D. S., Mueller, T. (2009). *Truncation and angular-scattering corrections for absorbing aerosol in the TSI 3563 Nephelometer.* Aerosol Sci. Technol. 43:866-871.

Bond, T. C., Doherty, S. J., Fahey, D. W., Forster, P. M., Berntsen, T., DeAngelo, B. J., Flanner, M. G., Ghan, S., Karcher, B., Koch, D., Kinne, S., Kondo, Y., Quinn, P. K., Sarofim, M. C., Schultz, M. G., Schulz, M., Venkataraman, C., Zhang, H., Zhang, S., Bellouin, N., Guttikunda, S. K., Hopke, P. K., Jacobson, M. Z., Kaiser, J. W., Klimont, Z., Lohmann, U., Schwarz, J. P., Shindell, D., Storelvmo, T., Warren, S. G., Zender, C. S. (2013). *Bounding the role of black carbon in the climate system: A scientific assessment*. J. Geophys. Res. Atmos. 118:5380-5552.

Bulatov, V.; Fisher, M.; Schechter, I. (2002). *Aerosol analysis by cavity-ring-down laser spectroscopy*. Analytica Chimica Acta. 466:1–9.

Butler, T. J. A., Miller, J. L., Orr-Ewing, A. J. (2007). Cavity ring-down spectroscopy measurements of single aerosol particle extinction. I. The effect of position of a particle within the laser beam on extinction. J. Chem. Phys. 126:174302.

Chow, J. C., Watson, J. G., Chen, L. W. A., Arnott, W. P., Moosmüller, H., and Fung, K. (2004). *Equivalence of elemental carbon by thermal/optical reflectance and transmittance with different temperature protocols*. *Environ. Sci. Technol., 38*: 4414–4422.

Collaud-Coen, M., Weingartner, E., Apituley, A., Ceburnis, D., Fierz-Schmidhauser, R., Flentje, H., Henzing, J. S., Jennings, S. G., Moerman, M., Petzold, A., Schmid, O., and

Baltensperger, U. (2010). *Minimizing light absorption measurement artifacts of the Aethalometer: evaluation of five correction algorithms*, Atmos. Meas. Tech., 3, 457–474, doi:10.5194/amt-3-457-2010.

Curtis, L. (2002). *Biomass burning: wood, leaves, grass, forests, corps and trash*. Burning Issues Special Edition, Fall Issue.

Fine, P. M.; Cass, G. R.; Simoneit, B. R. T. (2001). *Chemical characterization of fine particle emissions from fireplace combustion of woods grown in the Northeastern United States*. Environ. Sci. Technol,. 35 (13): 2665-2675.

Fine, P. M.; Cass, G. R.; Simoneit, B. R. T. (2002). *Chemical characterization of fine particle emissions from the fireplace combustion of woods grown in the Southern United States*. Environ. Sci. Technol. 36 (7): 1442-1451.

Fine, P.M., Cass, G.R., Simoneit, B.R.T. ( 2004a). *Chemical characterization of fine particulate emissions from the fireplace combustion of woods grown in the Midwestern and western United States*. Environmental Engineering Science 21, 387–409.

Fine, P.M., Cass, G.C., Simoneit, B.R.T. (2004b). *Chemical characterization of fine particle emissions from the wood stove combustion of prevalent United States tree species.* Environmental Engineering Science 21, 705–721.

Gerber, H. E. (1979). *Portable cell for simultaneously measuring the coefficients of light scattering and extinction for ambient aerosols*. Appl. Opt. 18. 1009-1014.

Gras, J., Meyer, C., Weeks, I., Gillett, R., Galbally, I., Todd, J., Carnovale, F., Joynt, R., Hinwood, A., Berko, H., Brown, S. (2002). *Technical Report No. 5: Emissions from Domestic Solid Fuel Burning Appliances*; Environment Australia: Canberra, www.deh.gov.au/atmosphere.

IPCC (2013). Climate Change 2013: The Physical Science Basis. Contribution of Working Group I to the Fifth Assessment Report of the Intergovernmental Panel on Climate Change, T. F. Stocker, D. Qin, G.-K. Plattner, M. Tignor, S. K. Allen, J. Boschung, A. Nauels, Y. Xia, V. Bex, P. M. Midgley, eds., Intergovernmental Panel on Climate Change, Cambridge, United Kingdom, 1535.

Hansen, A. D. A., Rosen, H., and Novakov, T. (1982). Real-time measurement of the absorption coefficient of aerosol particles, Appl.Opt., 21, 3060–3062, 1982.

Hansen, J. and Nazarenko, L. (2004). *Soot climate forcing via snow and ice albedos*. Proc. Natl. Acad. Sci. U.S.A 101:423-428.

Lack, D. A., Lovejoy, E. R., Baynard, T., Pettersson, A., and Ravishankara, A. R. (2006). *Aerosol absorption measurement using photoacoustic spectroscopy: Sensitivity, calibration, and uncertainty developments*, Aerosol Sci. Tech., 40, 697–708, doi:10.1080/02786820600803917.

Li, L., Chen, J., Chen, H., Yang, X., Tang, Y., Zhang, R. (2011). *Monitoring optical properties of aerosols with cavity ring-down spectroscopy*. J. Aerosol Sci. 42:277-284.

Massoli, P., Murphy, D. M., Lack, D. A., Baynard, T., Brock, C. A., Lovejoy, E. R. (2009). *Uncertainty in light scattering measurements by TSI Nephelometer: Results from laboratory studies and implications for ambient measurements*. Aerosol Sci. Technol. 42:1064-1074.

Mie, Gustav (1908). "Beiträge zur Optik trüber Medien, speziell kolloidaler Metallösungen". *Annalen der Physik* **330** (3): 377–445.

Miles, R. E. H., Rudic, S., Orr-Ewing, A. J., Reid, J. P. (2011). *Sources of error and uncertainty in the use of cavity ring down spectroscopy to measure aerosol optical properties*. Aerosol Sci. Technol. 45:1360-1375.

Mishchenko, M. I., Cairns, B., Hansen, J. E., Travis, L. D., Burg, R., Kaufman, Y. J., Martins, J. V., Shettle, E. P. (2004). *Monitoring of aerosol forcing of climate from space: Analysis of measurement requirements*. J. Quant. Spec. Rad. Transfer 88:149-161.

Mishchenko, M. I., Hovenier, J. W., Travis, L. D. (2000). *Light scattering by nonspherical particles: Theory, measurements, and applications*. Academic Press: San Diego, CA.

Mishchenko, M. I., Travis, L. D., Lacis, A. A. (2002). *Scattering, absorption, and emission of light by small particles*. Cambridge University Press: Cambridge, NY.

Moosmüller, H., Chakrabarty, R. K. , Arnott, W. P. (2009). *Aerosol light absorption and its measurement: A review*. Journal of Quantitative Spectroscopy & Radiative Transfer. *110*. 844-878, DOI: 10.1016/j.jqsrt.2009.02.035.

Müller, T., Henzing, J. S., de Leeuw, G., Wiedensohler, A.,Alastuey, A., Angelov, H., Bizjak, M., Collaud-Coen, M., Engstrom, J. E., Gruening, C., Hillamo, R., Hoffer, A., Imre, K., Ivanow, P., Jennings, G., Sun, J. Y., Kalivitis, N., Karlsson, H., Komppula, M., Laj, P., Li, S.-M., Lunder, C., Marinoni, A., Martins dos Santos, S., Moerman, M., Nowak, A., Ogren, J. A., Petzold, A., Pichon, J. M., Rodriquez, S., Sharma, S., Sheridan, P. J., Teinila, K., Tuch, T., Viana, M., Virkkula, A., Weingartner, E., Wilhelm, R., and Wang, Y. Q. (2011). *Characterization and intercomparison of aerosol absorption photometers: result of two intercomparison workshops*, Atmos. Meas. Tech., 4, 245–268, doi:10.5194/amt-4-245-2011.

Müller, T., Nowak, A., Wiedensohler, A., Sheridan, P., Laborde, M., Covert, D. S., Marinoni, A., Imre, K., Henzing, B., Roger, J.-C., dos Santos, S. M., Wilhelm, R., Wang, Y.-Q., de Leeuw, G. (2009). *Angular illumination and truncation of three different integrating nephelometers: Implications for empirical, size-based corrections*. Aerosol Sci. Technol. 43:581-586.

O'Keefe, A. and Deacon, D. A. G. (1988). *Cavity ring-down optical spectrometer for absorption measurements using pulsed laser source*s. Review of Scientific Instruments 59:2544-2551.

Pettersson, A., Lovejoy, E. R., Brock, C. A., Brown, S. S., Ravishankara, A. R. (2004). *Measurement of aerosol optical extinction at 532nm with pulsed cavity ring down spectroscopy*. J. Aerosol Sci. 35:995-1011.

Petzold, A., Ogren, J. A., Fiebig, Laj, M. P., Li, S.-M., Baltensperger, U., Holzer-Popp, T., Kinne, S., Pappalardo, G., Sugimoto, N., Wehrli, C., Wiedensohler, A., and Zhang, X.-Y. (2013). *Recommendations for reporting "black carbon" measurements.* Atmos. Chem. Phys., 13: 8365–8379.

Ramanathan, V. and Carmichael, G. (2008). *Global and regional climate changes due to black carbon*. Nature Geosci. 1:221-227.

Riziq, A. A., Trainic, M., Erlick, C. Segre, E., Rudich, Y. (2008). *Extinction efficiencies of coated absorbing aerosols measured by cavity ring down aerosol spectrometry*. Atmospheric Chemistry and Physics, 8. 1823-1833.

Saide, P.E., Spak, S., Pierce, B., Otkin, J., Rabin, R.M., Schaack,T., Heidinger, A., Da Silva, A., Kacenelenbogen, M., Redemann, J., and Carmichael, G. (2014). *Role of Central*

*American Biomass Burning smoke in increasing Tornado Severity in the US*, Abstract only, Bulletin of American Meteorological Society. Volume 95, Issue 7.

Sappey, A. D., Hill, E. S., Settersten, T., Linne, M. A. (1998). *Fixed-frequency cavity ringdown diagnostic for atmospheric particulate matter. Opt. Lett. 23*. 954-956.

Schmid, O., Artaxo, P., Arnott,W. P., Chand, D., Gatti, L. V., Frank, G. P., Hoffer, A., Schnaiter, M., and Andreae, M. O. (2006). *Spectral light absorption by ambient aerosols influenced by biomass burning in the Amazon Basin. I: Comparison and field calibration of absorption measurement techniques*, Atmos. Chem. Phys., 6, 3443–3462, doi:10.5194/acp-6-3443-2006.

Schmidl, C., Marr, I. L., Caseiro, A., Kotianova, P., Berner, A., Bauer,H., Kasper-Giebl,A., Puxbaum, H. (2011). *Chemical characterization of fine particle emissions from wood stove combustion of common woods growing in mid-European Alpine regions*. Atmospheric Environment doi:10.1016/j.atmosenv.2007.09.028.

Schwartz, S. E. and Lewis, E. R. (2012). *Interactive comment on Are black carbon and soot the same? by P. R. Buseck et al.: Disagreement on proposed nomenclature*, Atmos. Chem. Phys. Discuss., 12: C9099–C9109.

Sharma, N., Arnold, I. J., Moosmüller, H., Arnott, W. P., and Mazzoleni, C.(2013). *Photoacoustic and nephelometric spectroscopy of aerosol optical properties with a supercontinuum light source.* Atmos. Meas. Tech., 6, 3501-3513.

Singh, S.; Fiddler, M. N.; Smith, D.; Bililign, S. (2014). *Error analysis and uncertainty in the determination of aerosol optical properties using cavity ring-down spectroscopy, integrating nephelometry, and the extinction-minus-scattering method. In press* - Journal of Aerosol Science and Technology.

Smith, G. S. (2011). Estimate for the effect of forward scattering on the measurement of extinction for particles by cavity ringdown spectroscopy. Appl. Opt. 50:5422-5429.

Sorensen, C. M. (2001) *Light scattering by fractal aggregates: A review*. Aerosol Science and Technology, 3*5*. 648-687, DOI: 10.1080/02786820117868.

Tillman, D.A., Rossi, A.J., Kitto, W.D., (1981). *Wood Combustion: Principles, Processes, and Economics*. Academic Press: New York, NY.

Wang, J.; van den Heever S.C.; and Reid, J. (2013). *A conceptual model for the link between Central American biomass burning aerosols and severe weather over the south central United States***,** Environ. Res. Lett., 4**,** 15003.

Yokelson, R. J., Burling, I. R., Gilman, J. B., Warneke, C., Stockwell, C. E., de Gouw, J., Akagi, S. K., Urbanski, S. P., Veres, P., Roberts, J. M., Kuster, W. C., Reardon, J., Griffith, W. T., Johnson, T. J., Hosseini, S., Miller, J. W., Cocker III, D. R., Jung, H., Weise, D. R. (2013). *Coupling field and laboratory measurements to estimate the emission factors of identified and unidentified trace gases for prescribed fires*. Atmos. Chem. Phys., 13:89-116.

Yuan,T. (2014). *Evidence of anthropogenic increase of lightening over the Amazon. Sixth Symposium on Aerosol-Cloud-Climate Interactions*, Bulletin of American Meteorological Society, Volume 95, Issue 7.

Zalicki, P., Zare, R. N. (1995). *Cavity ring-down spectroscopy for quantitative absorption measurements*. J. Chem. Phys. *102*. 2708-2717, DOI: 10.1063/1.468647.

Zhang, R., Khalizov, A. F., Pagels, J., Zhang, D., Xue, H., McMurry, P. H. (2008). *Variability in morphology, hygroscopicity, and optical properties of soot aerosols during atmospheric*

*processing.* Proceedings of the National Academy of Sciences of the United States of America 105:10291-10296.